Monthly Notices
of the
ROYAL ASTRONOMICAL SOCIETY

Mon. Not. R. Astron. Soc. **406,** 1885–1906 (2010) doi:10.1111/j.1365-2966.2010.16800.x

47 new T dwarfs from the UKIDSS Large Area Survey

Ben Burningham,[1⋆] D. J. Pinfield,[1] P. W. Lucas,[1] S. K. Leggett,[2] N. R. Deacon,[3] M. Tamura,[4] C. G. Tinney,[5] N. Lodieu,[6,7] Z. H. Zhang,[1] N. Huelamo,[8] H. R. A. Jones,[1] D. N. Murray,[1] D. J. Mortlock,[9] M. Patel,[9] D. Barrado y Navascués,[8] M. R. Zapatero Osorio,[8] M. Ishii[10] M. Kuzuhara[11] and R. L. Smart[12]

[1]*Centre for Astrophysics Research, Science and Technology Research Institute, University of Hertfordshire, Hatfield AL10 9AB*
[2]*Gemini Observatory, 670 N. A'ohoku Place, Hilo, HI 96720, USA*
[3]*Institute for Astronomy, University of Hawaii, 2680 Woodlawn Drive, Honolulu, HI 96822, USA*
[4]*National Astronomical Observatory, Mitaka, Tokyo 181-8588, Japan*
[5]*School of Physics, University of New South Wales, NSW 2052, Australia*
[6]*Instituto de Astrofísica de Canarias, 38200 La Laguna, Spain*
[7]*Departamento de Astrofísica, Universidad de La Laguna, E-38205 La Laguna, Tenerife, Spain*
[8]*Centro de Astrobiologia (CSIC-INTA) E-28850 Torrejón de Ardoz, Madrid, Spain*
[9]*Astrophysics Group, Imperial College London, Blackett Laboratory, Prince Consort Road, London SW7 2AZ*
[10]*Subaru Telescope, 650 North A'ohoku Place, Hilo, Hi 96720, USA*
[11]*University of Tokyo, Hongo, Tokyo 113-0033, Japan*
[12]*Istituto Nazionale di Astrofisica, Osservatorio Astronomico di Torino, Strada Osservatrio 20, 10025 Pino Torinese, Italy*

Accepted 2010 April 2. Received 2010 March 3; in original form 2009 December 23

ABSTRACT

We report the discovery of 47 new T dwarfs in the Fourth Data Release (DR4) from the Large Area Survey (LAS) of the United Kingdom Infrared Telescope (UKIRT) Infrared Deep Sky Survey with spectral types ranging from T0 to T8.5. These bring the total sample of LAS T dwarfs to 80 as of DR4. In assigning spectral types to our objects we have identified eight new spectrally peculiar objects, and divide seven of them into two classes. H_2O-*H*-early have a H_2O-*H* index that differs with the H_2O-*J* index by at least two subtypes. CH_4-*J*-early have a CH_4-*J* index that disagrees with the H_20-*J* index by at least two subtypes. We have ruled out binarity as a sole explanation for both types of peculiarity, and suggest that they may represent hitherto unrecognized tracers of composition and/or gravity. Clear trends in $z'(AB) - J$ and $Y - J$ are apparent for our sample, consistent with weakening absorption in the red wing of the K I line at 0.77 μm with decreasing effective temperature. We have used our sample to estimate space densities for T6–T9 dwarfs. By comparing our sample to Monte Carlo simulations of field T dwarfs for various mass functions of the form $\psi(M) \propto M^{-\alpha}$ pc^{-3} M$_{\odot}^{-1}$, we have placed weak constraints on the form of the field mass function. Our analysis suggests that the substellar mass function is declining at lower masses, with negative values of α preferred. This is at odds with results for young clusters that have been generally found to have $\alpha > 0$.

Key words: surveys – brown dwarfs – stars: low-mass.

1 INTRODUCTION

The study of substellar objects presents a number of important opportunities for extending our understanding of star and planet formation, both through detailed study of individual systems and through statistical population studies. The statistical characteristics of the substellar population, such as binary fraction and distribution, and the form of the initial mass function (IMF; Salpeter 1955) across the entire substellar regime provide crucial observational constraints for models of star and planet formation, which currently offer a number of alternative formation scenarios that depend on differing balances of the dominant physics across the low-mass stellar–substellar mass spectrum (e.g. Bate & Bonnell 2005; Padoan & Nordlund 2002, and references therein). The crucial first step for any observational effort to address these issues is the initial identification of a statistically useful sample of brown dwarfs, the first of which were not discovered until the mid-1990s.

The majority of brown dwarfs have been identified via one of two routes: the mining of wide-field surveys such as the Sloan Digital

⋆E-mail: b.burningham@herts.ac.uk

Sky Survey (SDSS; York et al. 2000) and the Two Micron All Sky Survey (2MASS; Skrutskie et al. 2006) to find nearby L and T dwarf members of the field population and deep optical and near-infrared surveys of the young clusters and OB associations (e.g. Lucas & Roche 2000; Zapatero Osorio et al. 2000; Caballero et al. 2007; Bihain et al. 2009). Most recently, the United Kingdom Infrared Telescope (UKIRT) Infrared Deep Sky Survey (UKIDSS) Galactic Clusters Survey has significantly improved the substellar sample across a number of young regions (e.g. Lodieu, Hambly & Jameson 2006; Lodieu et al. 2007a, 2009).

To date, the results from clusters and associations have dominated the study of the low-mass extreme of the IMF due largely to the assumption of coevality in clusters that allows the mass–age degeneracy for substellar objects to be broken. A number of determinations have been published that are broadly in agreement across the $\sim$0.1–0.03 $M_{\odot}$ range (e.g. Barrado y Navascués et al. 2002; Moraux et al. 2003, 2007; Lodieu et al. 2009).

It is the age–mass degeneracy that has hampered efforts to measure the form of the substellar IMF from analysis of the local field population of L and T dwarfs. Although the determination of masses for individual field brown dwarfs is currently prevented by uncertainty about their age, the field mass function can still be constrained through comparison of the observed luminosity function or spectral type distribution with those predicted by Monte Carlo simulations for various star formation histories and underlying mass functions (e.g. Chabrier 2002; Burgasser 2004; Deacon & Hambly 2006). Allen et al. (2005) have applied a different statistical approach to solving this problem, by using Bayesian inference to evaluate the probabilities of different underlying mass functions for space densities of M, L and T dwarfs from 2MASS and SDSS, and estimated the age distribution of the field population.

Searches of the SDSS and 2MASS data sets have resulted in the discovery of over 500 L dwarfs and more than 100 T dwarfs in the field (see www.DwarfArchives.org for an up-to-date list of published objects). However, this sample is dominated by objects earlier than type T6, with just 26 objects identified in 2MASS and SDSS with types T6 or later and just a handful of type T8. And it is this population of objects in the $\geq$T6 range that is most sensitive to the underlying mass function, whilst the spectral type distribution of earlier objects depends more strongly on the Galactic formation history (see Burgasser 2004, fig. 5).

The Large Area Survey (LAS) of the UKIDSS has now successfully extended the T dwarf sample to types later than those first revealed by the 2MASS and SDSS surveys (Warren et al. 2007; Burningham et al. 2008, 2009) and is now identifying a substantial sample of late-type T dwarfs that will be ideal for constraining the substellar mass function in the field. In this paper we extend our searches of earlier data releases of the LAS [Lodieu et al. 2007b; Pinfield et al. 2008, Data Releases 1 and 2 (DR1 and DR2), respectively] to include all candidates drawn from DR4 (which incorporates DR1–DR3) which took place on 2008 July 1. Follow-up to confirm spectral types for this sample is now essentially complete for $J \leq 19.0$ and we report here the discovery of 47 new T dwarfs, including one T8+ dwarf and a number of spectrally peculiar objects, and use this sample to place improved constraints on the form of the field substellar mass spectrum.

2 SOURCE IDENTIFICATION

Candidate T dwarfs were selected from UKIDSS LAS DR3 and DR4 following a method similar to that described in Lodieu et al. (2007b), Pinfield et al. (2008) and Burningham et al. (2008, 2009).

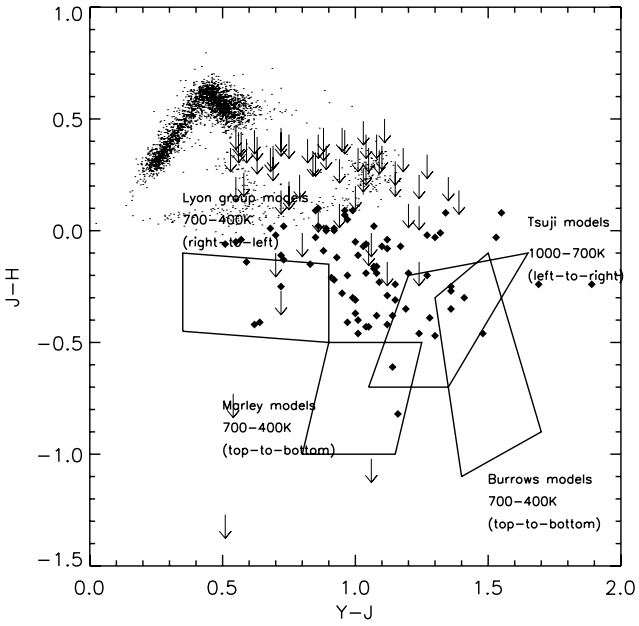

Figure 1. DR4 T dwarf candidates plotted on a *YJH* colour–colour plot. *YJH*-selected candidates are shown as diamonds, whilst objects that are undetected in *H* in UKIDSS DR4 are shown as upper limits in *JH*. The photometry is that from the UKIDSS survey.

The UKIDSS project is defined in Lawrence et al. (2007), and uses the UKIRT Wide Field Camera (WFCAM; Casali et al. 2007). The photometric system is described in Hewett et al. (2006). The pipeline processing and science archive are described by Irwin et al. (2004) and Hambly et al. (2008).

Initial candidate selection is based on the presence of blue $J - H$ and $J - K$ colours ($\leq$0.1) and red $z' - J$ (>3.0, or non-detection in SDSS DR7). Since the LAS has nominal 5σ limits of 18.8 and 18.4 in the *H* and *K* bands, respectively (cf. 20.5 and 20.0 for *Y* and *J*), we ensure that we are complete to a faint cut-off at $J = 19.3$ by further selecting sources that are detected in *YJ*, but are undetected in *HK*, and also have $z' - J > 3.0$, or are undetected in SDSS DR7 (we only consider sources that lie within the SDSS footprint). In the case of the sources that are undetected in *H* and *K*, we also impose a $Y - J > 0.5$ requirement, to help eliminate contamination from earlier type M dwarfs near the faint limit of our selection.

To monitor for the existence of T dwarfs with $Y - J < 0.5$, we do not impose a $Y - J$ colour cut on our *YJH*-selected candidates. However, following the cross-match against SDSS no candidates with $Y - J < 0.5$ remain in the sample (see Fig. 1). We thus infer that the *YJ* criterion for *H* and *K* non-detections should not exclude any T dwarfs.

Candidates were then followed up photometrically to remove contamination and determine accurate magnitudes across the full *zYJHK* range where possible. In 700 deg^2 of DR3 and DR4 LAS sky [excluding 280 deg^2 of DR1 and DR2 sky already searched by Lodieu et al. (2007b) and Pinfield et al. (2008)], our initial SDSS + UKIDSS based selection identified 83 candidates with *YJH* detections (black diamonds in Fig. 1) and 80 candidates with *YJ*-only detections (indicated with arrows in Fig. 1), with $J < 19.3$.

Our follow-up is most complete for targets with $J < 19.0$, of which there were 55 *YJH* candidates and 17 *YJ*-only candidates. Of the 55 *YJH* candidates, photometric follow-up revealed three to be likely solar system objects (SSOs) which had apparently moved since the original survey were taken, and five were found to be

objects with $J - H > 0.1$ that had been scattered into our selection by either photometric error or intrinsic variability (*YJ* and *JH* data were often taken at different epochs). Of the remaining 47 targets, 46 have been confirmed as T dwarfs and one still requires spectroscopic confirmation, 38 are presented here and eight have been previously published elsewhere (Burningham et al. 2008; Delorme et al. 2008; Pinfield et al. 2008; Burningham et al. 2009). Of the 17 *YJ*-only candidates with $J < 19.0$, four were found to be likely SSOs, seven were found to be objects with $J - H > 0.1$ but whose *H*-band magnitude was beyond the *H*-band limit of the LAS. Five have been confirmed as T dwarfs, and one target still requires photometric follow-up.

Although the follow-up of the $J > 19.0$ portion of our candidate list is less complete, it is predictably dominated by contamination caused by photometric scatter. Of the 25 *YJH* candidates with $J > 19.0$ that have been followed up photometrically, 22 have revised $J - H > 0.1$. For the *YJ*-only selection we find that of the 24 sources with $J < 19.0$ that have been followed up, 18 have $J - H > 0.1$, whilst two are likely SSOs.

The photometric follow-up required significant investment of observing time, dominated by deep *H*-band imaging of objects fainter than $J = 19.0$, which required 1-h integrations to achieve 10 per cent photometry on 4-m class facilities, while brighter candidates typically required 20–30 min integrations for similar results. All objects that passed the photometric follow-up stage were spectroscopically confirmed as T dwarfs.

2.1 Near-infrared photometry

Near-infrared follow-up photometry was obtained using the UKIRT Fast Track Imager (UFTI; Roche et al. 2003) mounted on UKIRT, and the Long-slit Infrared Imaging Spectrograph (LIRIS; Manchado et al. 1998) mounted on the William Herschel Telescope on La Palma, across a number of observing runs spanning 2007–2009. The final image mosaics were produced using sets of jittered images, with individual exposure times, jitter patterns and number of repeats given in Appendix A along with the dates of the observations. The data were dark subtracted, flat-field corrected, sky subtracted and mosaicked using ORAC-DR for the UFTI data and LIRIS-DR for the LIRIS data.

Data were obtained in a variety of observing conditions across the runs from photometric conditions with stable, subarcsecond seeing to thin cirrus with variable seeing. Under the photometric conditions photometric calibration was achieved using a standard star observed at similar airmass. Observations taken under non-photometric conditions were calibrated against 2MASS stars within the field of view.

The resulting photometry for the new T dwarfs discussed here is presented on the MKO system in Table 1. Where no follow-up photometry was obtained (mainly in the *Y* and *K* bands) the survey photometry is supplied instead. Data obtained on the LIRIS system were converted to the MKO system using transforms given in Pinfield et al. (2008) and Burningham et al. (2009). Appendix A lists the instruments used and dates for all sources described here, along with details of the conditions.

2.2 Optical photometry

We obtained optical *z*-band photometry using the European Southern Observatory (ESO) Multi-Mode Instrument (EMMI) mounted on the New Technology Telescope (NTT) at La Silla, Chile under programme 080.C-0090 and also using the ESO Faint Object Spectrograph and Camera (EFOSC2), also on the NTT, under programmes 081.C-0552 and 082.C-0399. The details of the observations for each target are given in Appendix A. The data were reduced using standard IRAF packages, and then multiple images of the same target were aligned and stacked to increase signal-to-noise ratio. The zero-points were determined by using SDSS stars as secondary calibrators. The uncertainty we quote for our *z*-band photometry incorporates a scatter of $\sim\pm0.05$ in the determined zero-points.

For the EMMI follow-up, which used a Bessel *z*-band filter (ESO Z#611), we used the transform given by Warren et al. (2007) to calculate $z_{\rm EMMI}$ for the fiducial SDSS stars. The resulting EMMI photometry was then transformed to the Sloan $z'(AB)$ system (see Warren et al. 2007).

For the EFOSC2 observations, for which a Gunn *z*-band filter (ESO Z#623) was used, we used the transform given in Burningham et al. (2009) to calculate $z_{\rm EFOSC2}$ for the secondary calibrators. To place the resulting $z_{\rm EFOSC2}(AB)$ photometry on the Sloan $z'(AB)$ system, we synthesized photometry for the T dwarf spectral standards (Burgasser et al. 2006), finding that across the T3–T8 range $z_{\rm EFOSC2}(AB) - z'(AB) = -0.19 \pm 0.02$, which is similar to the offset calculated by Warren et al. (2007) for $z_{\rm EMMI}(AB) - z'(AB) = -0.2$.

The resulting photometry, on the $z'(AB)$ system, is given in Table 1.

3 SPECTROSCOPIC CONFIRMATION

3.1 Observations and data reduction

Spectroscopic confirmation of those candidates that survived the photometric follow-up programme was achieved using the Near-InfraRed Imager and Spectrometer (NIRI; Hodapp et al. 2003) on the Gemini North Telescope [1] and the InfraRed Camera and Spectrograph (IRCS; Kobayashi et al. 2000) on the Subaru telescope, both on Mauna Kea, Hawaii. All observations were made up of a set of subexposures in an ABBA jitter pattern to facilitate effective background subtraction, with a slit width of 1 arcsec. The length of the AB jitter was 10 arcsec. The details of individual observations are summarized in Appendix A. The NIRI observations were reduced using standard IRAF Gemini packages. The Subaru IRCS *JH* spectrum was also extracted using standard IRAF packages. The AB pairs were subtracted using generic IRAF tools, and median stacked.

Comparison argon arc frames were used to obtain dispersion solutions, which were then applied to the pixel coordinates in the dispersion direction on the images. The resulting wavelength-calibrated subtracted pairs had a low level of residual sky emission removed by fitting and subtracting this emission with a set of polynomial functions fit to each pixel row perpendicular to the dispersion direction, and considering pixel data on either side of the target spectrum only. The spectra were then extracted using a linear aperture, and cosmic rays and bad pixels removed using a sigma-clipping algorithm.

Telluric correction was achieved by dividing each extracted target spectrum by that of an early A or F type star observed just before or after the target and at a similar airmass. Prior to division, hydrogen lines were removed from the standard star spectrum by interpolating the stellar continuum. Relative flux calibration was then achieved by multiplying through by a blackbody spectrum of the appropriate $T_{\rm eff}$. Data obtained for the same spectral regions on different nights

[1] Under programmes GN-2007B-Q-26, GN-2008A-Q-15, GN-2008B-Q-29 and GN-2009A-Q-16.

Table 1. The 'best' selection of photometry for each of the new ultracool dwarfs, in most cases this is the result of the follow-up photometry described in Sections 2.1 and 2.2. However, in some cases this is the UKIDSS survey photometry; these data are marked with a superscript 'u'.

Object	α (J2000)	δ (J2000)	Type	$z'(AB)$	Y	J	H	K	$z'(AB)-J$	$Y-J$	$J-H$	$H-K$
ULAS J0150+1359	01:50:24.37	13:59:24.00	T7.5	21.79 ± 0.21	18.80 ± 0.06^{u}	17.73 ± 0.02	18.11 ± 0.02	17.84 ± 0.16^{u}	4.06 ± 0.20	1.07 ± 0.06	-0.38 ± 0.03	0.27 ± 0.16
ULAS J0200+1337	02:00:47.44	13:37:55.10	T4	22.15 ± 0.15	19.83 ± 0.13^{u}	18.78 ± 0.03	19.22 ± 0.03	–	3.37 ± 0.14	1.05 ± 0.14	-0.44 ± 0.04	–
ULAS J0209+1339	02:09:44.30	13:39:24.70	T5.5	22.12 ± 0.19	19.80 ± 0.12^{u}	18.35 ± 0.03	18.64 ± 0.03	–	3.77 ± 0.18	1.45 ± 0.13	-0.29 ± 0.04	–
ULAS J0819+0733	08:19:48.09	07:33:23.30	T6p	21.93 ± 0.08	19.36 ± 0.04	18.24 ± 0.03	18.36 ± 0.03	18.33 ± 0.04	3.69 ± 0.07	1.12 ± 0.05	-0.12 ± 0.04	0.03 ± 0.05
ULAS J0840+0759	08:40:36.72	07:59:33.60	T4.5	22.54 ± 0.10	19.98 ± 0.11^{u}	19.04 ± 0.08	19.40 ± 0.09	–	3.50 ± 0.12	0.94 ± 0.14	-0.36 ± 0.12	–
ULAS J0842+0936	08:42:11.68	09:36:11.90	T5.5	22.09 ± 0.09	19.58 ± 0.18^{u}	18.38 ± 0.02	18.84 ± 0.02	19.08 ± 0.18	3.71 ± 0.07	1.20 ± 0.18	-0.46 ± 0.03	-0.24 ± 0.18
ULAS J0851+0053	08:51:39.03	00:53:40.90	T4	22.30 ± 0.10	20.12 ± 0.02	18.80 ± 0.02	18.96 ± 0.02	19.01 ± 0.03	3.50 ± 0.10	1.32 ± 0.03	-0.16 ± 0.03	-0.05 ± 0.04
ULAS J0853+0006	08:53:42.94	00:06:51.80	T6p	23.60 ± 0.35	19.78 ± 0.11^{u}	18.63 ± 0.03	19.21 ± 0.06	19.26 ± 0.13	4.97 ± 0.35	1.15 ± 0.11	-0.58 ± 0.07	-0.05 ± 0.14
ULAS J0857+0913	08:57:15.96	09:13:25.30	T6	21.69 ± 0.08	19.57 ± 0.18^{u}	18.56 ± 0.03	18.89 ± 0.10	18.62 ± 0.20^{u}	3.13 ± 0.07	1.01 ± 0.18	-0.33 ± 0.10	0.27 ± 0.22
ULAS J0926+0711	09:26:24.76	07:11:40.70	T3.5	20.74 ± 0.06	18.52 ± 0.02	17.48 ± 0.02	17.41 ± 0.02	17.88 ± 0.06	3.26 ± 0.04	1.04 ± 0.03	0.07 ± 0.03	-0.47 ± 0.06
ULAS J0926+0835	09:26:05.47	08:35:17.00	T4.5	22.16 ± 0.09	19.86 ± 0.15^{u}	18.57 ± 0.02	18.69 ± 0.01	19.14 ± 0.25	3.59 ± 0.07	1.29 ± 0.15	-0.12 ± 0.02	-0.45 ± 0.25
ULAS J0929+1105	09:29:26.44	11:05:47.30	T2	22.67 ± 0.10	20.45 ± 0.16^{u}	19.08 ± 0.02	19.1 ± 0.02	–	3.59 ± 0.09	1.37 ± 0.16	-0.02 ± 0.03	–
ULAS J0943+0858	09:43:31.49	08:58:49.20	T5p	22.08 ± 0.09	19.67 ± 0.12^{u}	18.60 ± 0.02	18.54 ± 0.06	18.42 ± 0.18^{u}	3.48 ± 0.08	1.07 ± 0.12	0.06 ± 0.06	0.12 ± 0.19
ULAS J0943+0942	09:43:49.60	09:42:03.40	T4.5p	22.42 ± 0.09	19.88 ± 0.14	18.84 ± 0.05	18.80 ± 0.03	–	3.58 ± 0.09	1.04 ± 0.15	0.04 ± 0.06	–
ULAS J0945+0755	09:45:16.39	07:55:45.60	T5	21.16 ± 0.06	18.75 ± 0.03	17.49 ± 0.02	17.71 ± 0.03	17.75 ± 0.06	3.67 ± 0.04	1.26 ± 0.04	-0.22 ± 0.03	-0.04 ± 0.07
ULAS J1012+1021	10:12:43.54	10:21:01.70	T5.5	20.67 ± 0.07	18.00 ± 0.02	16.87 ± 0.01	17.21 ± 0.02	17.55 ± 0.05	3.80 ± 0.05	1.13 ± 0.02	-0.34 ± 0.02	-0.33 ± 0.05
ULAS J1034−0015	10:34:34.52	-00:15:53.00	T6.5p	–	20.73 ± 0.28^{u}	18.86 ± 0.03	19.00 ± 0.03	–	–	1.87 ± 0.28	-0.14 ± 0.04	–
ULAS J1052+0016	10:52:35.42	00:16:32.70	T5	22.29 ± 0.25	20.24 ± 0.32^{u}	18.83 ± 0.03	18.69 ± 0.02	–	3.46 ± 0.25	1.41 ± 0.32	0.14 ± 0.04	–
ULAS J1149−0143	11:49:25.58	-01:43:43.20	T5	–	19.29 ± 0.07^{u}	18.11 ± 0.03	18.17 ± 0.03	18.34 ± 0.20	–	1.18 ± 0.08	-0.06 ± 0.04	-0.17 ± 0.20
ULAS J1153−0147	11:53:38.74	-01:47:24.10	T6	–	19.10 ± 0.03	17.59 ± 0.02	17.97 ± 0.02	17.83 ± 0.02	–	1.51 ± 0.04	-0.38 ± 0.03	0.14 ± 0.03
ULAS J1157−0139	11:57:18.02	-01:39:23.90	T5	–	19.52 ± 0.09^{u}	18.18 ± 0.02	18.65 ± 0.03	–	–	1.34 ± 0.09	-0.47 ± 0.04	–
ULAS J1202+0901	12:02:57.05	09:01:58.80	T5	20.48 ± 0.07	18.00 ± 0.02	16.71 ± 0.03	16.91 ± 0.02	16.94 ± 0.02	3.77 ± 0.06	1.29 ± 0.04	-0.20 ± 0.04	-0.03 ± 0.03
ULAS J1207+1339	12:07:44.65	13:39:02.70	T6	–	19.19 ± 0.05	18.28 ± 0.05	18.52 ± 0.05	18.67 ± 0.05	–	0.91 ± 0.07	-0.24 ± 0.07	-0.15 ± 0.07
ULAS J1231+0912	12:31:53.60	09:12:05.40	T4.5p	22.42 ± 0.16	20.12 ± 0.2^{u}	19.03 ± 0.10^{u}	19.13 ± 0.23^{u}	–	3.39 ± 0.18	1.09 ± 0.22	-0.10 ± 0.25	–
ULAS J1233+1219	12:33:27.45	12:19:52.20	T3.5	21.70 ± 0.11	19.22 ± 0.05	17.87 ± 0.03	18.28 ± 0.06	19.03 ± 0.06	3.83 ± 0.10	1.35 ± 0.06	-0.41 ± 0.07	-0.75 ± 0.08
ULAS J1239+1025	12:39:03.75	10:25:18.60	T0	22.24 ± 0.30	19.49 ± 0.08^{u}	18.50 ± 0.06^{u}	18.40 ± 0.03	–	3.74 ± 0.31	0.99 ± 0.10	0.10 ± 0.07	–
ULAS J1248+0759	12:48:04.56	07:59:04.00	T7	–	18.81 ± 0.03	17.72 ± 0.02^{u}	18.15 ± 0.08	18.06 ± 0.03^{u}	–	1.09 ± 0.04	-0.43 ± 0.08	0.09 ± 0.09
ULAS J1257+1108	12:57:08.07	11:08:50.40	T4.5	22.25 ± 0.30	19.38 ± 0.11^{u}	18.39 ± 0.03	18.51 ± 0.03	–	3.86 ± 0.30	0.99 ± 0.11	-0.12 ± 0.04	–
ULAS J1302+1308	13:02:17.21	13:08:51.20	T8.5	22.61 ± 0.30	19.12 ± 0.03	18.11 ± 0.04	18.60 ± 0.06	18.28 ± 0.03	4.50 ± 0.30	1.01 ± 0.05	-0.49 ± 0.07	0.32 ± 0.07
ULAS J1319+1209	13:19:43.77	12:09:00.20	T5p	–	20.39 ± 0.05	18.90 ± 0.05	18.90 ± 0.15	19.41 ± 0.10	–	1.49 ± 0.07	0.00 ± 0.16	-0.51 ± 0.18
ULAS J1320+1029	13:20:48.12	10:29:10.60	T5	21.48 ± 0.14	18.97 ± 0.06^{u}	17.82 ± 0.02	17.89 ± 0.05^{u}	18.17 ± 0.13^{u}	3.66 ± 0.13	1.15 ± 0.06	-0.07 ± 0.05	-0.28 ± 0.14
ULAS J1326+1200	13:26:05.18	12:00:09.90	T6p	–	18.73 ± 0.03	17.50 ± 0.02	17.93 ± 0.09	17.58 ± 0.05	–	1.23 ± 0.04	-0.43 ± 0.09	0.35 ± 0.10
ULAS J1349+0918	13:49:40.81	09:18:33.30	T7	–	20.51 ± 0.03	19.16 ± 0.03	19.43 ± 0.03	19.37 ± 0.04	–	1.35 ± 0.04	-0.27 ± 0.04	0.06 ± 0.05
ULAS J1356+0853	13:56:07.41	08:53:45.20	T5	22.03 ± 0.16	19.37 ± 0.05	18.04 ± 0.05	18.19 ± 0.03	18.22 ± 0.05	3.99 ± 0.16	1.33 ± 0.07	-0.15 ± 0.06	-0.03 ± 0.06
ULAS J1444+1055	14:44:58.87	10:55:31.10	T5	–	19.78 ± 0.10^{u}	18.82 ± 0.04	18.91 ± 0.03	–	–	0.96 ± 0.11	-0.09 ± 0.05	–
ULAS J1445+1257	14:45:55.24	12:57:35.10	T6.5	22.54 ± 0.24	20.03 ± 0.04	18.56 ± 0.05	19.10 ± 0.05	19.05 ± 0.04	3.98 ± 0.24	1.47 ± 0.06	-0.54 ± 0.07	0.05 ± 0.06
ULAS J1459+0857	14:59:35.25	08:57:51.20	T4.5	21.42 ± 0.19	19.24 ± 0.06	17.98 ± 0.04	17.93 ± 0.04	18.04 ± 0.03	3.44 ± 0.18	1.26 ± 0.07	0.05 ± 0.06	-0.11 ± 0.05

Table 1 – *continued*

Object	α (J2000)	δ (J2000)	Type	$z'(AB)$	Y	J	H	K	$z'(AB)-J$	$Y-J$	$J-H$	$H-K$
ULAS J1525+0958	15:25:26.25	09:58:14.30	T6.5	–	19.70 ± 0.11″	18.54 ± 0.03	19.17 ± 0.03	–	–	1.16 ± 0.11	−0.63 ± 0.04	–
ULAS J1529+0922	15:29:12.23	09:22:28.50	T6	22.20 ± 0.21	20.16 ± 0.12″	18.61 ± 0.03	19.13 ± 0.05	–	3.59 ± 0.20	1.55 ± 0.13	−0.52 ± 0.06	–
ULAS J2256+0054	22:56:49.51	00:54:52.50	T4.5	22.10 ± 0.21	19.39 ± 0.11″	18.83 ± 0.09	19.07 ± 0.1	–	3.27 ± 0.22	0.56 ± 0.14	−0.24 ± 0.13	–
ULAS J2306+1302	23:06:01.02	13:02:25.00	T6.5	21.58 ± 0.11	18.96 ± 0.03	17.57 ± 0.02	18.00 ± 0.02	18.03 ± 0.03	4.01 ± 0.10	1.39 ± 0.04	−0.43 ± 0.03	−0.03 ± 0.04
ULAS J2315+1322	23:15:57.61	13:22:56.20	T6.5	21.48 ± 0.16	18.83 ± 0.03	17.71 ± 0.05	18.16 ± 0.05	18.14 ± 0.03	3.77 ± 0.16	1.13 ± 0.07	−0.45 ± 0.07	0.02 ± 0.07
ULAS J2318−0013	23:18:35.51	-00:13:30.00	T4.5	22.58 ± 0.24	19.89 ± 0.08	18.84 ± 0.05	19.25 ± 0.06	19.41 ± 0.11	3.74 ± 0.25	1.05 ± 0.09	−0.41 ± 0.08	−0.16 ± 0.13
ULAS J2320+1448	23:20:35.28	14:48:29.80	T5	20.65 ± 0.11	18.14 ± 0.02	16.79 ± 0.02	17.14 ± 0.02	17.40 ± 0.02	3.86 ± 0.10	1.35 ± 0.03	−0.35 ± 0.03	−0.26 ± 0.03
ULAS J2321+1354	23:21:23.79	13:54:54.90	T7.5	21.08 ± 0.16	17.92 ± 0.03	16.72 ± 0.03	17.15 ± 0.03	17.16 ± 0.01	4.36 ± 0.15	1.20 ± 0.04	−0.43 ± 0.04	−0.01 ± 0.03
ULAS J2328+1345	23:28:02.03	13:45:44.80	T7	21.99 ± 0.16	19.01 ± 0.02	17.75 ± 0.02	18.17 ± 0.02	18.29 ± 0.02	4.24 ± 0.15	1.26 ± 0.03	−0.42 ± 0.03	−0.12 ± 0.03
ULAS J2348+0052	23:48:27.94	00:52:20.50	T5	21.95 ± 0.11	19.80 ± 0.15	18.68 ± 0.03	18.99 ± 0.03	–	3.27 ± 0.10	1.12 ± 0.15	−0.31 ± 0.04	–

were co-added after relative flux calibration, each weighted by their exposure time.

Initial, short, *J*- or *JH*-band spectra were used to establish an object's status as a T dwarf. In cases where the initial spectrum was suggestive of a late type, or the target had unusual colours for its type, deeper *J*-band and *H*- and *K*-band spectra were also obtained, and joined together using the measured near-infrared photometry to place the spectra on an absolute flux scale. In the case of Subaru/IRCS spectra, the red end of the spectra taken with the *JH* grism overlaps with blueward limit of the spectra taken with the *HK* grism. We were able to use the overlap region in the *H* band to bring the spectra on to a common flux scale for joining. Complete details of the spectroscopic observations obtained for each of the T dwarfs presented here are given in Appendix A. The resulting spectra are shown in Fig. 2.

3.2 Spectral types

Spectral types have been determined through by-eye comparison to spectral type templates, and by measuring spectral type indices for the T sequence laid out in Burgasser et al. (2006) and extended by Burningham et al. (2008) for the latest types. The indices used here are summarized in Table 2. The final adopted type is arrived at by consideration of the determined indices and the best template match. The template comparison is generally given as much weight as the combined result of the indices. However, in cases where only two non-degenerate typing indices are available, and they disagree, the template comparison type is adopted. Fig. 3 shows the values of the computing indices plotted against adopted type for the sample presented here, along with previously identified T dwarfs.

The results of this process are given in Table 3. In cases where spectroscopy is available across the entire *JHK* range, the uncertainties in the types are ±0.5 subtypes. In the majority of cases, however, we only have coverage in *J* or *JH*, and in these cases the precision drops to ±1 subtype.

Two objects in our selection have recently been independently identified as T dwarfs by Goldman et al. (2010): ULAS J1149−0143 and ULAS J1153−0147. Using methane imaging they estimate spectral types of T5 ± 1.5 and T6.5 ± 1 for these objects, respectively. These estimates agree well with our derived spectral types of T5 and T6 (±1).

3.3 Peculiar classifications

We have classified six objects as peculiar in Table 3, as indicated by the postscript 'p' on their assigned type. There are essentially two routes to classification as peculiar: (i) a mismatch of two or more subtypes between the results of the different spectral typing ratios; (ii) other specific anomalies in the spectrum as compared to the template spectrum for the adopted type. Of the seven objects classified as peculiar in Table 3, all exhibit a spectral type mismatch.

The mismatch of spectral types implied by different indices has been seen before. In Pinfield et al. (2008), the T6.5p dwarf ULAS J1150+0949 displayed a T3-like H_2O-*H* index, whilst displaying later types in all other indices. The T8p dwarf ULAS J1017+0118 (Burningham et al. 2008) displays a similar mismatch, with indices consistent with T8 classification in the *J* band, but T6-like indices in the *H* and *K* bands. Gl 229B displays T5-like indices in H_2O-*H*, and CH_4-*K*, a T6-like H_2O-*J* and T7-like CH_4-*J* and CH_4-*H* (Burgasser et al. 2006).

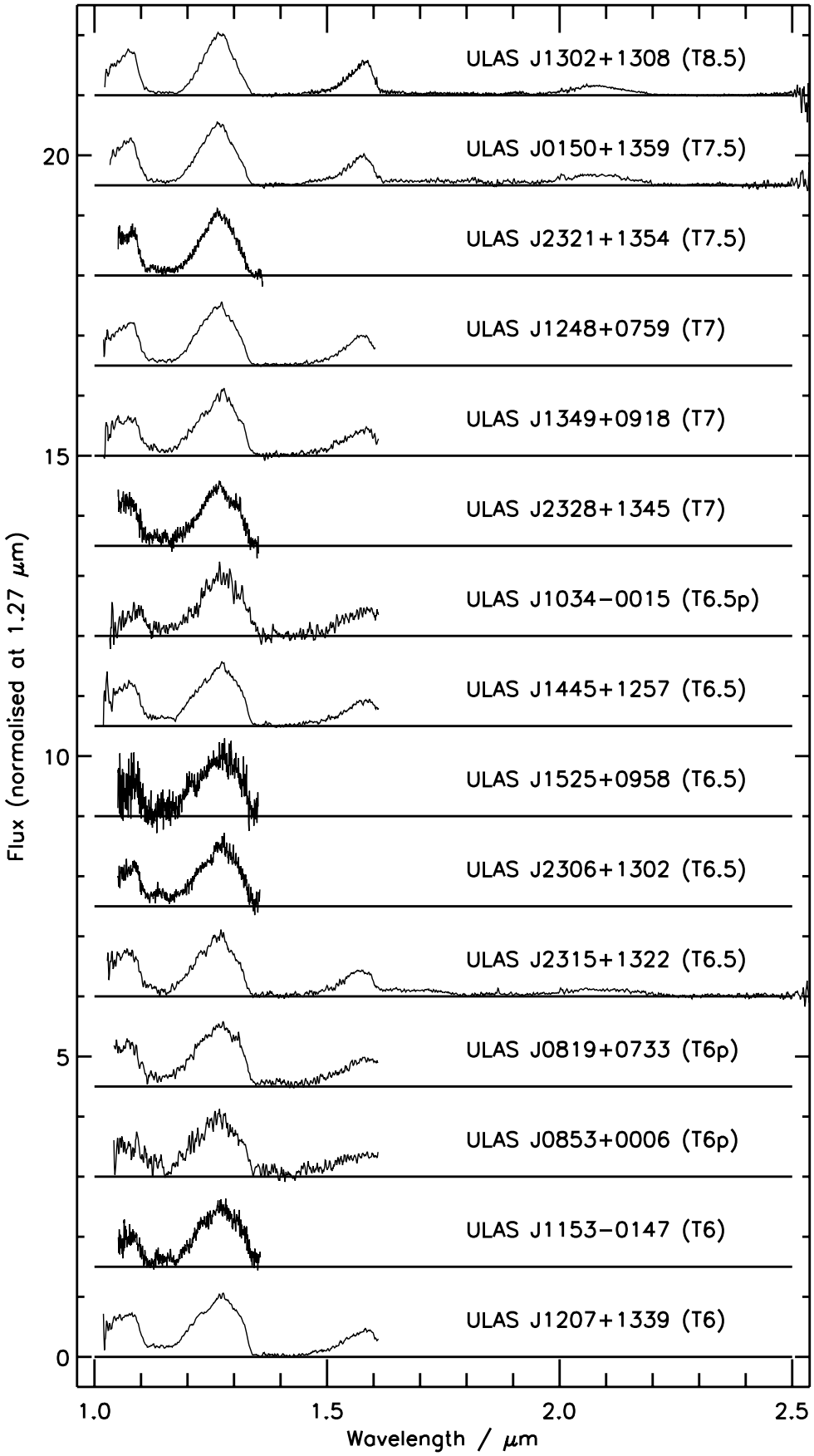

Figure 2. Spectra of the 47 T dwarfs presented here. Each spectrum is normalized at 1.27 ± 0.005 μm and offset for clarity. The spectra have been rebinned by a factor of 3 to maximize signal-to-noise ratio whilst not sacrificing resolution.

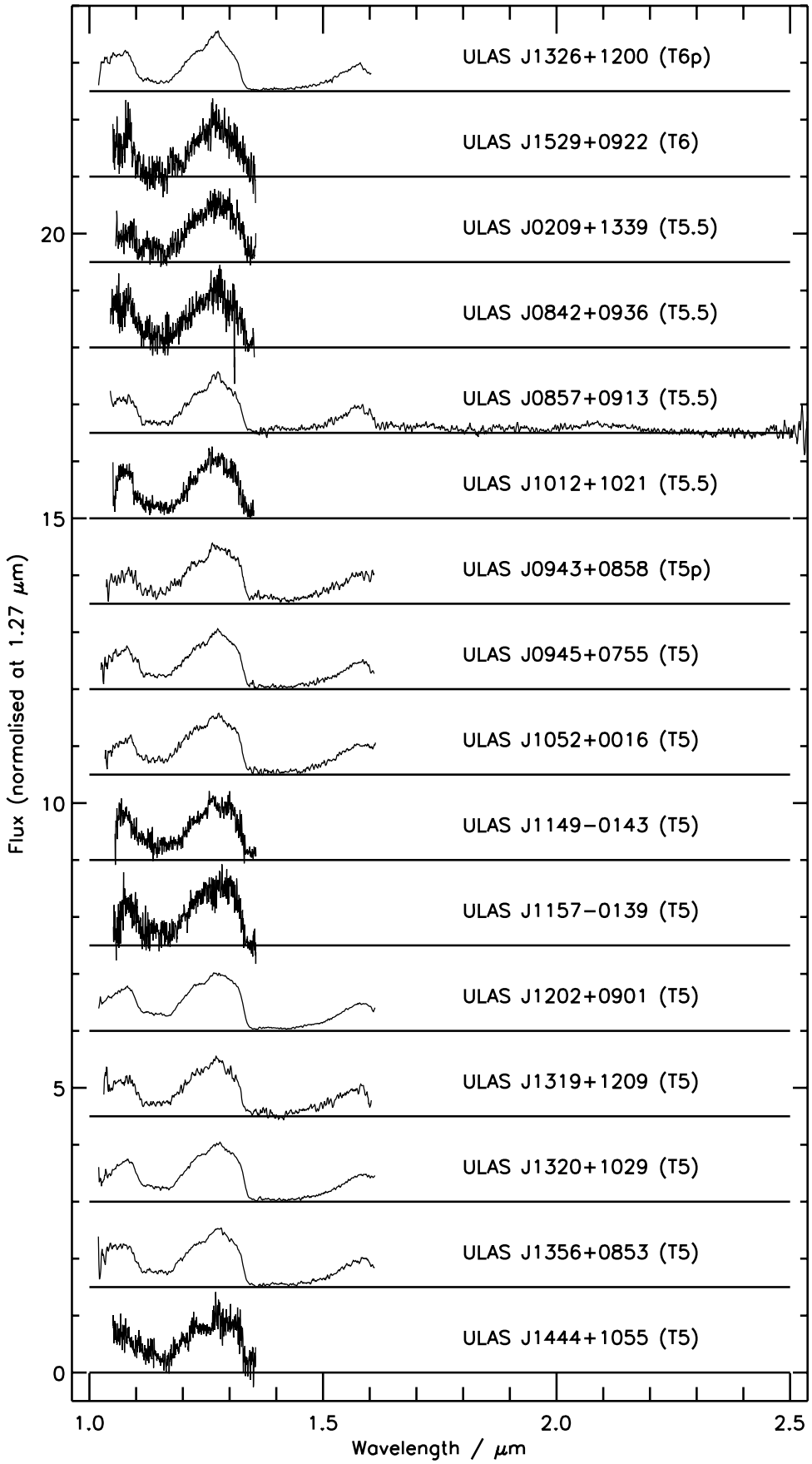

Figure 2 – *continued*

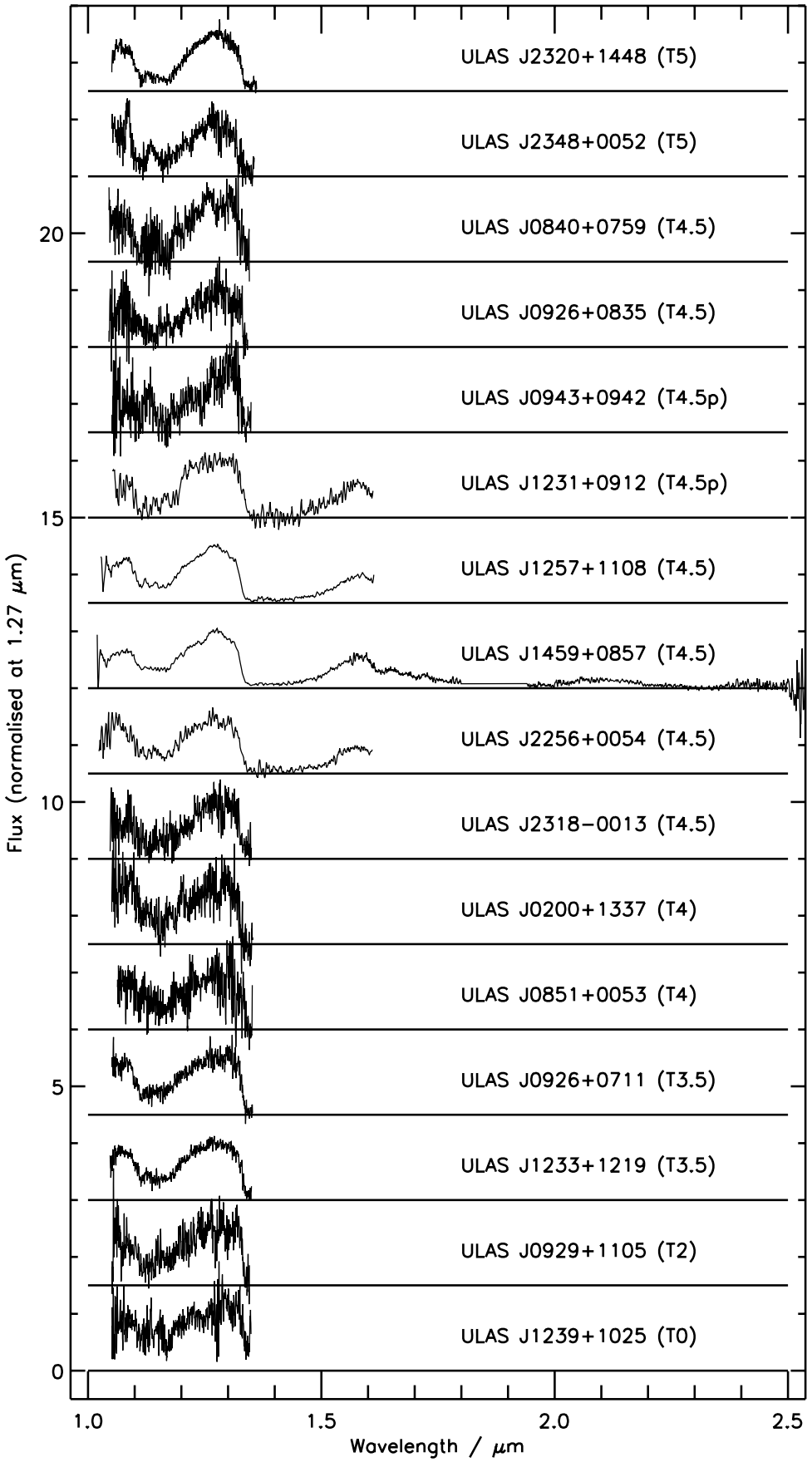

Figure 2 – *continued*

Table 2. The indices used for spectral typing the sample presented here. This follows the system for T0–T8 dwarfs described by (Burgasser et al. 2006) and extended to T9 by (Burningham et al. 2008) using the W_J index suggested by Warren et al. (2007).

Type	H_2O-J $\frac{\int_{1.14}^{1.165} f(\lambda)d\lambda}{\int_{1.26}^{1.285} f(\lambda)d\lambda}$	CH_4-J $\frac{\int_{1.315}^{1.34} f(\lambda)d\lambda}{\int_{1.26}^{1.285} f(\lambda)d\lambda}$	W_J $\frac{\int_{1.18}^{1.23} f(\lambda)d\lambda}{2\int_{1.26}^{1.285} f(\lambda)d\lambda}$	H_2O-H $\frac{\int_{1.48}^{1.52} f(\lambda)d\lambda}{\int_{1.56}^{1.60} f(\lambda)d\lambda}$	CH_4-H $\frac{\int_{1.635}^{1.675} f(\lambda)d\lambda}{\int_{1.56}^{1.60} f(\lambda)d\lambda}$	CH_4-K $\frac{\int_{2.215}^{2.255} f(\lambda)d\lambda}{\int_{2.08}^{2.12} f(\lambda)d\lambda}$
T0	–	0.73–0.78	–	0.60–0.66	0.97–1.00	0.75–0.85
T1	>0.55	0.67–0.73	–	0.53–0.60	0.92–0.97	0.63–0.75
T2	0.45–0.55	0.58–0.67	–	0.46–0.53	0.80–0.92	0.55–0.63
T3	0.38–0.45	0.52–0.58	–	0.43–0.46	0.60–0.80	0.35–0.55
T4	0.32–0.38	0.45–0.52	–	0.37–0.43	0.48–0.60	0.24–0.35
T5	0.18–0.32	0.36–0.45	–	0.32–0.37	0.36–0.48	0.18–0.24
T6	0.13–0.18	0.28–0.36	–	0.26–0.32	0.25–0.36	0.13–0.18
T7	0.07–0.13	0.21–0.28	0.35–0.40	0.20–0.26	0.15–0.25	<0.13
T8	<0.07	<0.21	0.28–0.35	0.14–0.20	<0.15	–
T9	–	–	<0.28	<0.14	–	–

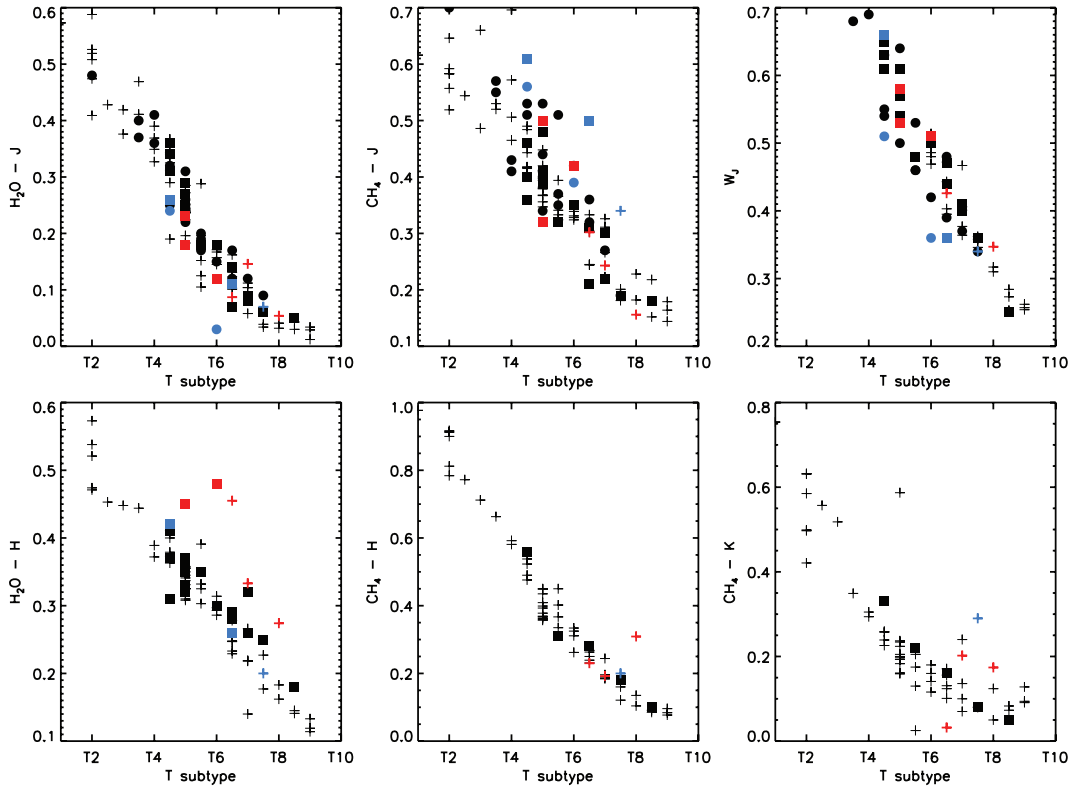

Figure 3. Adopted spectral types plotted against computed index values (see Table 2) for the sample presented here, and previously published T dwarfs from Burgasser et al. (2006), Warren et al. (2007), Lodieu et al. (2007b), Delorme et al. (2008), Burningham et al. (2008), Pinfield et al. (2008), Burningham et al. (2009) and Burningham et al. (2010). Previously published T dwarfs are indicated with '+' symbols. Types derived from NIRI spectra are indicated by circles and from IRCS data by squares. Blue symbols represent CH_4-J-early peculiar objects, whilst red symbols indicate H_2O-H-early peculiarity. Colour version of figure is available in on-line version.

In the sample presented here, the peculiar objects can be broadly separated into two classes. For the purposes of this discussion we define these as follows.

H_2O-H-early: H_2O-H index implies an earlier type than that suggested by the H_2O-J index by at least two subtypes (see Fig. 4).

CH_4-J-early: CH_4-J index implies an earlier type than that suggested by the H_20-J index by at least two subtypes (see Fig. 5).

Figs 6 and 7 show comparisons of the indices that define these peculiarities. In both cases the peculiar objects are apparent as outliers. It is also apparent that not all outliers have been classified as peculiar. This is due to the fact that the peculiarities have been defined with respect to the spectral index bins for each subtype, the size of which is not the same for all subtypes and differs between the ratios themselves. As a result an object can appear as an outlier in Figs 6 and 7, although its index values might be consistent to within a subtype. The definitions of the peculiarities described above may, in the future, require refinement but for now will serve as reasonable starting points for highlighting the objects that exhibit the most obvious peculiar features.

In addition to the two objects already published, we have identified two T6p objects and two T5p objects which display H_2O-H-early peculiarity. One additional peculiar object has been identified

Table 3. Spectral typing ratios for the confirmed T dwarfs as set out by Burgasser et al. (2006) and Burningham et al. (2009), along with the types from template comparison and the final adopted types. A superscript '*J*' indicates that and object has been typed as CH_4-*J*-early peculiar, whilst a superscript '*H*' indicates H_2O-*H*-early peculiarity (see text).

Name	SpSource	Adopted	Templ.	H_2O-*J*	CH_4-*J*	W_J	H_2O-*H*	CH_4-*H*	CH_4-*K*
ULAS J0150+1359	IRCS	T7.5	T7.5	0.06 ± 0.01 (>T7)	0.19 ± 0.01 (>T7)	0.36 ± 0.01 (T7/8)	0.25 ± 0.01 (T6/7)	0.18 ± 0.01 (T7)	0.08 ± 0.01 (>T6)
ULAS J0200+1337	NIRI	T4	T4	0.36 ± 0.03 (T4)	0.41 ± 0.03 (T5)	0.75 ± 0.03 (<T7)	–	–	–
ULAS J0209+1339	NIRI	T5.5	T5	0.19 ± 0.02 (T5/6)	0.51 ± 0.02 (T3/4)	0.53 ± 0.01 (<T7)	–	–	–
ULAS J0819+0733	IRCS	T6p^H	T6	0.16 ± 0.01 (T6)	0.38 ± 0.01 (T5)	0.49 ± 0.01 (<T7)	0.40 ± 0.01 (T4)	–	–
ULAS J0840+0759	NIRI	T4.5	T4.5	0.25 ± 0.04 (T5)	0.51 ± 0.04 (T4)	0.63 ± 0.03 (<T7)	–	–	–
ULAS J0842+0936	NIRI	T5.5	T6	0.17 ± 0.02 (T5/6)	0.35 ± 0.02 (T5/6)	0.46 ± 0.02 (<T7)	–	–	–
ULAS J0851+0053	NIRI	T4	T4	0.41 ± 0.04 (T3/4)	0.43 ± 0.03 (T4/5)	0.69 ± 0.03 (<T7)	–	–	–
ULAS J0853+0006	IRCS	T6p^H	T6	0.12 ± 0.02 (T6/7)	0.42 ± 0.01 (T5)	0.51 ± 0.02 (<T7)	0.48 ± 0.04 (T2/3)	–	–
ULAS J0857+0913	IRCS	T5.5	T6	0.18 ± 0.01 (T5/6)	0.32 ± 0.01 (T6)	0.48 ± 0.01 (<T7)	0.35 ± 0.01 (T5)	0.31 ± 0.01 (T6)	0.22 ± 0.03 (T5)
ULAS J0926+0835	NIRI	T4.5	T5	0.32 ± 0.02 (T4/5)	0.53 ± 0.02 (T3/4)	0.55 ± 0.02 (<T7)	–	–	–
ULAS J0926+0711	NIRI	T3.5	T4	0.40 ± 0.01 (T3)	0.57 ± 0.01 (T3)	0.71 ± 0.01 (<T7)	–	–	–
ULAS J0929+1105	NIRI	T2	T2	0.48 ± 0.03 (T2)	0.70 ± 0.03 (T1)	0.71 ± 0.03 (<T7)	–	–	–
ULAS J0943+0858	IRCS	T5p^H	T5	0.18 ± 0.01 (T5/6)	0.50 ± 0.01 (T4)	0.53 ± 0.01 (<T7)	0.45 ± 0.01 (T3)	–	–
ULAS J0943+0942	NIRI	T4.5p^J	T4.5	0.24 ± 0.02 (T5)	0.56 ± 0.03 (T3)	0.51 ± 0.02 (<T7)	–	–	–
ULAS J0945+0755	IRCS	T5	T5	0.24 ± 0.01 (T5)	0.41 ± 0.01 (T5)	0.53 ± 0.01 (<T7)	0.36 ± 0.01 (T5)	–	–
ULAS J1012+1021	NIRI	T5.5	T5.5	0.20 ± 0.01 (T5)	0.37 ± 0.01 (T5/6)	0.46 ± 0.01 (<T7)	–	–	–
ULAS J1034−0015	IRCS	T6.5p^J	T6.5p	0.11 ± 0.02 (T7)	0.50 ± 0.02 (T4)	0.36 ± 0.01 (T7)	0.26 ± 0.03 (T6)	–	–
ULAS J1052+0016	IRCS	T5	T5	0.25 ± 0.01 (T5)	0.39 ± 0.01 (T5)	0.61 ± 0.01 (<T7)	0.37 ± 0.01 (T4/5)	–	–
ULAS J1149−0143	NIRI	T5	T5	0.26 ± 0.01 (T5)	0.4 ± 0.01 (T5)	0.5 ± 0.01 (<T7)	–	–	–
ULAS J1153−0147	NIRI	T6	T6	0.15 ± 0.01 (T6)	0.42 ± 0.01 (T5)	0.42 ± 0.01 (<T7)	–	–	–
ULAS J1157−0139	NIRI	T5	T5.5	0.24 ± 0.02 (T5)	0.41 ± 0.02 (T5)	0.54 ± 0.02 (<T7)	–	–	–
ULAS J1202+0901	IRCS	T5	T5	0.29 ± 0.01 (T5)	0.48 ± 0.01 (T4)	0.61 ± 0.01 (<T7)	0.35 ± 0.01 (T5)	–	–
ULAS J1207+1339	IRCS	T6	T6	0.18 ± 0.01 (T5/6)	0.35 ± 0.01 (T6)	0.50 ± 0.01 (<T7)	0.30 ± 0.01 (T6)	–	–
ULAS J1231+0912	IRCS	T4.5p^J	T4.5	0.26 ± 0.03 (T5)	0.61 ± 0.02 (T2)	0.66 ± 0.02 (<T7)	0.42 ± 0.03 (T3/4)	–	–
ULAS J1233+1219	NIRI	T3.5	T3.5	0.37 ± 0.01 (T3/4)	0.55 ± 0.01 (T3/4)	0.69 ± 0.01 (<T7)	–	–	–
ULAS J1239+1025	NIRI	T0	T0	0.65 ± 0.03 (<T1)	0.87 ± 0.03 (<T0)	0.82 ± 0.03 (<T7)	–	–	–
ULAS J1248+0759	IRCS	T7	T7	0.09 ± 0.01 (T7)	0.22 ± 0.01 (T7/8)	0.41 ± 0.01 (<T7/T7)	0.26 ± 0.01 (T6/7)	–	–
ULAS J1257+1108	IRCS	T4.5	T5	0.31 ± 0.01 (T4/5)	0.36 ± 0.01 (T5/6)	0.61 ± 0.01 (<T7)	0.37 ± 0.01 (T4/5)	–	–
ULAS J1302+1308	IRCS/NIRI	T8.5	T8.5	0.05 ± 0.01 (>T7)	0.18 ± 0.01 (>T7)	0.25 ± 0.01 (T9)	0.18 ± 0.01 (T8)	0.10 ± 0.01 (>T7)	0.05 ± 0.01 (>T6)
ULAS J1319+1209	IRCS	T5p^H	T5p	0.23 ± 0.01 (T5)	0.32 ± 0.01 (T6)	0.58 ± 0.01 (<T7)	0.45 ± 0.02 (T3)	–	–
ULAS J1320+1029	IRCS	T5	T5	0.25 ± 0.01 (T5)	0.48 ± 0.01 (T4)	0.54 ± 0.01 (<T7)	0.32 ± 0.01 (T5/6)	–	–
ULAS J1326+1200	IRCS	T6p	T6	0.16 ± 0.01 (T6)	0.25 ± 0.01 (T7)	0.50 ± 0.01 (<T7)	0.35 ± 0.01 (T5)	–	–
ULAS J1349+0918	IRCS	T7	T7	0.08 ± 0.01 (T7)	0.30 ± 0.01 (T6)	0.40 ± 0.01 (T7)	0.32 ± 0.01 (T5/6)	–	–
ULAS J1356+0853	IRCS	T5	T5	0.27 ± 0.01 (T5)	0.40 ± 0.01 (T5)	0.57 ± 0.01 (<T7)	0.33 ± 0.01 (T5)	–	–
ULAS J1444+1055	NIRI	T5	T5	0.25 ± 0.02 (T5)	0.53 ± 0.02 (T3/4)	0.64 ± 0.02 (<T7)	–	–	–

Table 3 – *continued*

Name	SpSource	Adopted	Templ.	H_2O-J	CH_4-J	W_J	H_2O-H	CH_4-H	CH_4-K
ULAS J1445+1257	IRCS	T6.5	T6.5	0.14 ± 0.01 (T6/7)	0.31 ± 0.01 (T6)	0.44 ± 0.01 (<T7)	0.28 ± 0.01 (T6)	–	–
ULAS J1459+0857	IRCS	T4.5	T4.5	0.34 ± 0.01 (T4)	0.40 ± 0.01 (T5)	0.63 ± 0.01 (<T7)	0.41 ± 0.01 (T4)	0.56 ± 0.01 (T4)	0.33 ± 0.02 (T4)
ULAS J1525+0958	NIRI	T6.5	T6.5	0.12 ± 0.02 (T7)	0.36 ± 0.02 (T5/6)	0.48 ± 0.02 (<T7)	–	–	–
ULAS J1529+0922	NIRI	T6	T6	0.03 ± 0.01 (>T7)	0.39 ± 0.02 (T5)	0.36 ± 0.01 (T7)	–	–	–
ULAS J2256+0054	IRCS	T4.5	T4.5	0.36 ± 0.02 (T4)	0.46 ± 0.02 (T4/5)	0.65 ± 0.02 (<T7)	0.31 ± 0.03 (T5/6)	–	–
ULAS J2306+1302	NIRI	T6.5	T6.5	0.17 ± 0.01 (T6)	0.32 ± 0.01 (T6)	0.39 ± 0.01 (T7)	–	–	–
ULAS J2315+1322	NIRI+IRCS	T6.5	T6.5	0.07 ± 0.01 (T7/8)	0.21 ± 0.01 (T7/8)	0.47 ± 0.01 (<T7	0.29 ± 0.01 (T6)	0.28 ± 0.01 (T6)	0.16 ± 0.02 (T6)
ULAS J2318−0013	NIRI	T4.5	T4.5	0.34 ± 0.02 (T4/5)	0.46 ± 0.03 (T4/5)	0.54 ± 0.03 (<T7)	–	–	–
ULAS J2320+1448	NIRI	T5	T5	0.22 ± 0.01 (T5)	0.44 ± 0.01 (T5)	0.54 ± 0.01 (<T7)	–	–	–
ULAS J2321+1354	NIRI	T7.5	T7.5	0.09 ± 0.01 (T7)	0.19 ± 0.01 (>T7)	0.34 ± 0.01 (T7/8)	–	–	–
ULAS J2328+1345	NIRI	T7	T7	0.12 ± 0.01 (T7)	0.27 ± 0.01 (T7)	0.37 ± 0.01 (T7)	–	–	–
ULAS J2348+0052	NIRI	T5	T5	0.31 ± 0.02 (T4/5)	0.34 ± 0.02 (T6)	0.57 ± 0.02 (<T7)	–	–	–

for which the CH_4-J index disagrees with the H_2O-H index, and as such does not fall within the two classes of peculiarity defined above.

For objects near the L–T transition, the combination of an earlier spectral type in the H band than that seen in the J band can be caused by unresolved binarity. In these cases the secondary T dwarf dominates in the J band due to the J-band brightening observed through the early T sequence (T1–T5) (e.g. Dahn et al. 2002; Tinney, Burgasser & Kirkpatrick 2003; Vrba et al. 2004), whilst the primary contributes more flux in the H band (e.g. Looper et al. 2008). This scenario is a potential explanation for the unusual spectral properties of ULAS J0943+0858 and ULAS J1319+1209, which both appear as T5 in the J band, but T3 in the H band.

To assess if this is the origin of the H_2O-H-early peculiarity seen in our sample, we have simulated various combinations of L8+T binaries (since the local minimum is L8 for M_J in the L–T transition providing the maximum boost to the secondary) and have found that a combination of a T6 and an L8 dwarf can produce a similar combination of spectral type indices as seen in ULAS J0943+0858. However, it requires the T6 to be at least 0.75 mag brighter than the L8 dwarf, and as such it would be a significant outlier on the M_J versus spectral type produced by Dahn et al. (2002), Tinney et al. (2003) and Vrba et al. (2004). Given the difficulty in producing a T5p through unresolved binarity, it comes as little surprise that we are also unable to simulate the T6p dwarfs by this mechanism. Since binarity alone is unlikely to cause H_2O-H-early peculiarity, we speculate that this morphology may instead represent an as-yet unidentified tracer of composition and/or surface gravity.

Of the four CH_4-J-early peculiar objects identified here, the 1.25 μm K I doublet is apparently absent from two (ULAS J1231+0912 and ULAS J1034−0015); however, the quality of the spectra are too poor to rule out its presence. Given such a small sample of objects displaying peculiarity of this type, interpretation of its significance is problematic. Additionally, the low signal-to-noise ratio of these spectra raises the possibility that the peculiarity is merely a product of poor-quality spectra.

The steep gradient and low flux in the spectrum in the region for the denominator of the CH_4-J index suggests that this peculiarity may in some cases be spurious. For example, the initial discovery spectrum of ULAS J1233+1219 displayed apparent CH_4-J-early peculiarity. However, the subsequent deeper follow-up spectrum resulted in spectral typing indices that were in agreement (although the red side of the J-band peak still appears somewhat earlier in type than the indices would otherwise imply). Although these issues are of concern, the presence of CH_4-J-early peculiarity in higher signal-to-noise ratio spectra (e.g. Burningham et al. 2010) argues for its inclusion with the types assigned in this paper.

Higher signal-to-noise ratio spectra of the peculiar objects identified here will establish the significance of the peculiarities discussed above. Determination of their kinematic properties should also be a priority, allowing for identification of any wide common proper-motion companions capable of providing fiducial constraints on metallicity and age.

3.4 ULAS J1302+1308 – a new T8.5 dwarf

Our newly expanded sample of LAS T dwarfs includes a new T8.5 dwarf, ULAS J1302+1308. This objects brings the number of published T8+ objects to six (Warren et al. 2007; Burningham et al. 2008; Delorme et al. 2008; Burningham et al. 2009). With a growing sample of all late-type objects we thus return to the question of the presence of ammonia absorption at 1.58 μm, first suggested

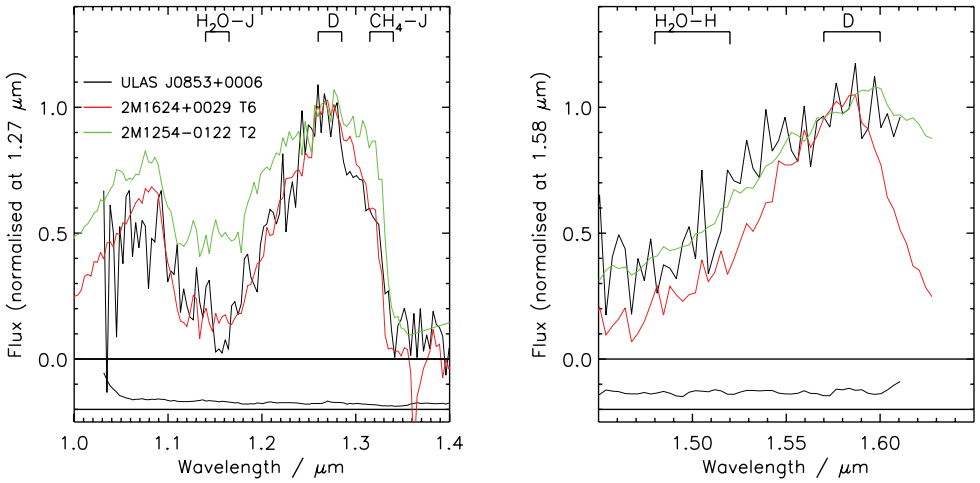

Figure 4. The spectrum of the H_2O-*H*-early T6p dwarf ULAS J0853+0006, plotted with spectra for the T6 and T2 spectral templates. The error spectrum for ULAS J0853+0006 is shown as a black line offset below the zero flux line.

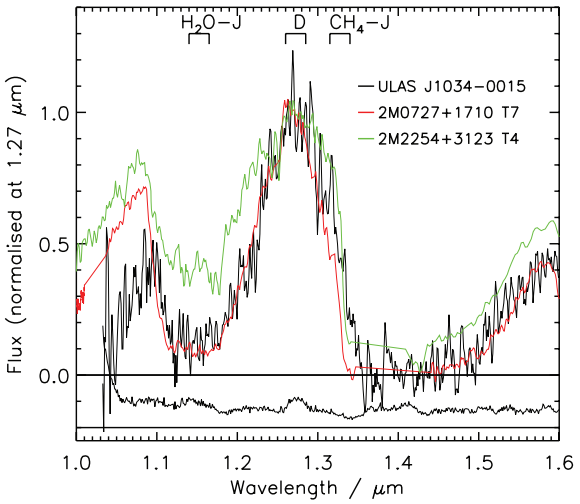

Figure 5. The spectrum of CH_4-*J*-early peculiar T7p dwarf ULAS J1034−0015 compared to the T7 template 2MASS J0727+1710. The error spectrum for ULAS J1034−0015 is shown as a black line offset below the zero flux line.

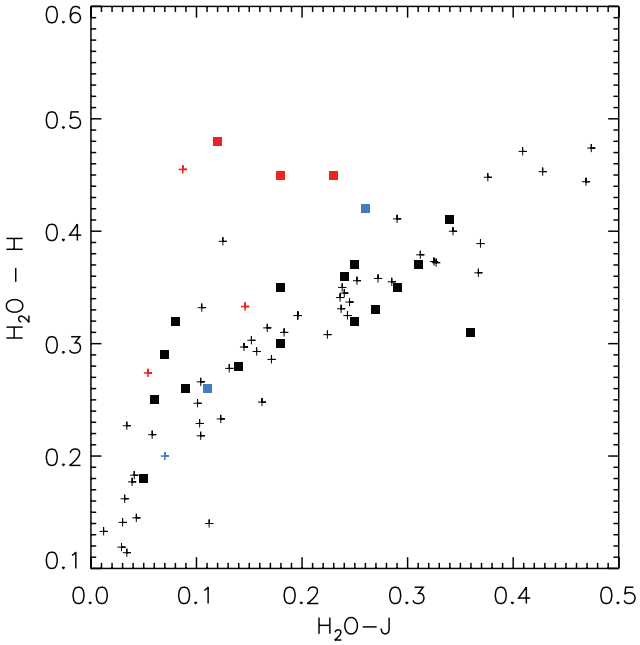

Figure 6. A comparison of the H_2O-*J* and H_2O-*H* spectral typing indices for the T dwarfs presented here and those published elsewhere. Symbols are as for Fig. 3.

by Delorme et al. (2008). In Fig. 8 we plot the suggested 'NH_3'-*H* index of Delorme et al. (2008) against spectral type [on the Burgasser et al. (2006) and Burningham et al. (2008) system]. Whilst this supports the assertion that the new index is effective at distinguishing the latest type objects, it does not strongly suggest the introduction of a new opacity source at later types. The trend is very much a continuation (with a similar degree of scatter) of that seen at earlier types, where opacity in this region is largely attributed to water vapour.

4 THE NEAR-INFRARED COLOURS OF UKIDSS T DWARFS

In addition to the 47 new T dwarfs presented here, we will consider all T dwarfs thus far published that lie within the LAS DR4 footprint (Kendall et al. 2007; Lodieu et al. 2007b; Warren et al. 2007; Burningham et al. 2008; Chiu et al. 2008; Delorme et al. 2008; Pinfield et al. 2008; Burningham et al. 2009), giving a total of 80 objects with spectral types from T0 to T9. Fig. 9 shows various far-red and near-infrared colours plotted as a function of spectral type.

Most striking is the wide scatter present in all colours for late-T dwarfs. This indicates that within each spectral type there is significant diversity of properties such as $T_{\rm eff}$, gravity and metallicity. However, trends with increasing spectral type are apparent in some colours, suggesting changes that are driven principally by decreasing $T_{\rm eff}$. It can be seen that the trends in $Y - J$ and $J - H$ already noted by Leggett et al. (2010) are reflected in our expanded sample. Also confirmed is the wide scatter in $H - K$ and $J - K$. A number of objects are noteworthy on these latter two plots as lying blueward of the bulk population. These objects may be members of a low-metallicity population and we defer detailed examination of these objects' spectra and kinematics to a future work (Murray et al., in preparation).

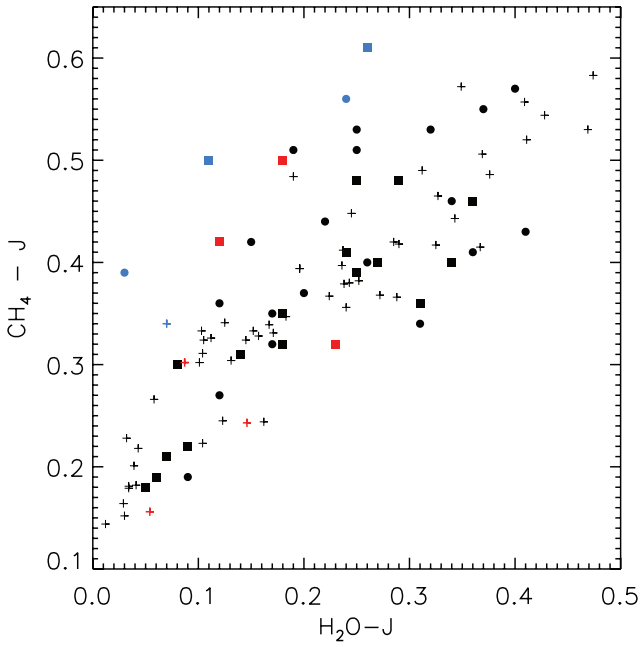

Figure 7. A comparison of the H_2O-*J* and CH_4-*J* spectral typing indices for the T dwarfs presented here and those published elsewhere. Symbols are as for Fig. 3.

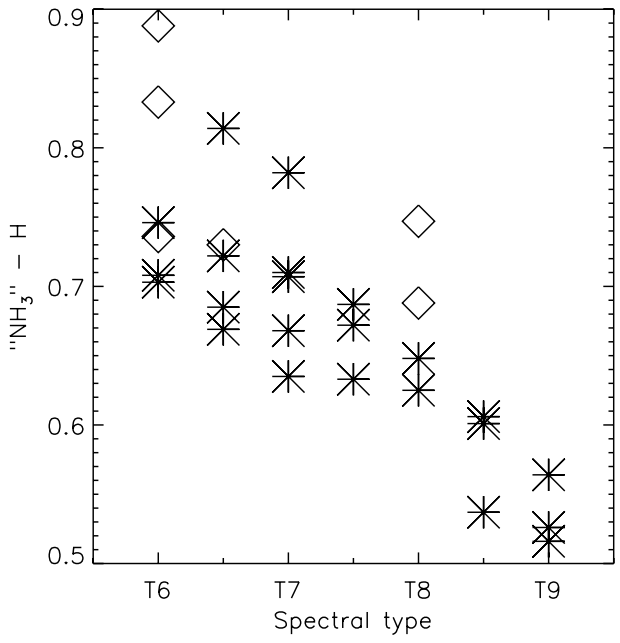

Figure 8. The 'NH_3'-*H* index for T6–T9 dwarfs classified on the system of Burgasser et al. (2006), extended to late types by Burningham et al. (2009). The plotted values incorporate objects described in this paper and previously published objects (Burgasser et al. 2006; Looper, Kirkpatrick & Burgasser 2007; Warren et al. 2007; Burningham et al. 2008; Delorme et al. 2008; Burningham et al. 2009). Index values for the latter have been calculated from the objects' spectra supplied by the authors. Uncertainties in the index are smaller than the symbol size, whilst uncertainties in the spectral type are typically ±0.5 subtypes. The open diamond symbols indicate objects classified as peculiar.

There appears to be a weak continuation of the trend of reddening $z' - J$ with type seen in earlier type objects (e.g. Chiu et al. 2006), but thus far undetected for the latest spectral types (Pinfield et al. 2008), presumably due to its broad scatter and the previously small sample size in this range. Most interesting, however, is the relatively strong trend in $z' - Y$ for ≥T6 dwarfs, coupled with decreasing $Y - J$ in the same regime. The latter has been noted elsewhere (e.g. Leggett et al. 2010); however, it was not previously clear if this was caused by depression of the *J*-band peak, or brightening in the *Y* band. The combined trends seen in Fig. 9 suggest the brightening of the *Y* band is responsible. This is most likely due to the broad K I absorption at 0.77 μm weakening as K I condenses into KCl (Lodders 1999).

We have also indicated the objects classified as peculiar in Section 3. Although some of the peculiar objects are clear outliers from the bulk population, the majority appear to have fairly typical colours for their types. There is also no apparent distinction between the two flavours of peculiarity discussed in Section 3. Unfortunately, we only have *K*-band photometry for one of the CH_4-*J*-early peculiar objects. This object has extremely blue $H - K$, consistent with the low-metallicity/high-gravity interpretation of its spectral morphology. Clearly more complete photometry, and better spectral coverage, for these unusual objects is required before sound physical interpretation of their properties will be possible.

5 CONSTRAINING THE SUBSTELLAR MASS FUNCTION

In Pinfield et al. (2008) comparison of the DR2 sample of ≥T4 dwarfs with the simulations of Deacon & Hambly (2006) allowed weak constraints to be placed on the substellar field IMF, favouring $\alpha \leq 0$ for an IMF of the form $\Psi\ (M) \propto M^{-\alpha}$. The increased volume probed by our DR4 sample allows us to now examine for the first time the constraints that may be drawn from a ≥T6 sample.

5.1 The sample

The sample of T dwarfs considered below represents all LAS T dwarfs that have been spectroscopically confirmed from 980 deg^2 of DR4 sky. All candidates with $J < 19.0$ and confirmed $J - H < 0.1$ that arose in our selection have been followed up, with the exception of one source. The source is a target from our so-called *YJ*-only search with $J = 18.8$. Contamination at this magnitude for the *YJ*-only search is typically worse than 60 per cent, so we do not include this object in our final sample. The total number of T dwarfs identified to date in LAS DR4 sky with $J - H < 0.1$ is 80 (Burgasser et al. 2004; Lodieu et al. 2007b; Burningham et al. 2008; Delorme et al. 2008; Pinfield et al. 2008; Burningham et al. 2009). Of these 31 have $J = 18.5$–19.0 and 42 have $J < 18.5$. If our sample were essentially complete to $J = 19.0$, we would expect our sample size to double with an increased depth of 0.5 mag (since this doubles the survey volume). It thus seems likely that our sample is not complete for late-T dwarfs to $J = 19.0$, as had been claimed by Pinfield et al. (2008), and we instead restrict our analysis to a brighter sample.

By selecting T dwarfs with $J \leq 18.8$ we find that 25 have $18.3 \leq 18.8$ and 36 with $J < 18.3$. Assuming Poisson noise, these numbers are roughly consistent with a similar level of completeness in the two bins, although it is likely that we are somewhat incomplete in the fainter bin. The completeness of our T dwarf sample is set by the *Y*-band completeness which is the fainter of our required detections in *Y* and *J*. Completeness as a function of signal-to-noise

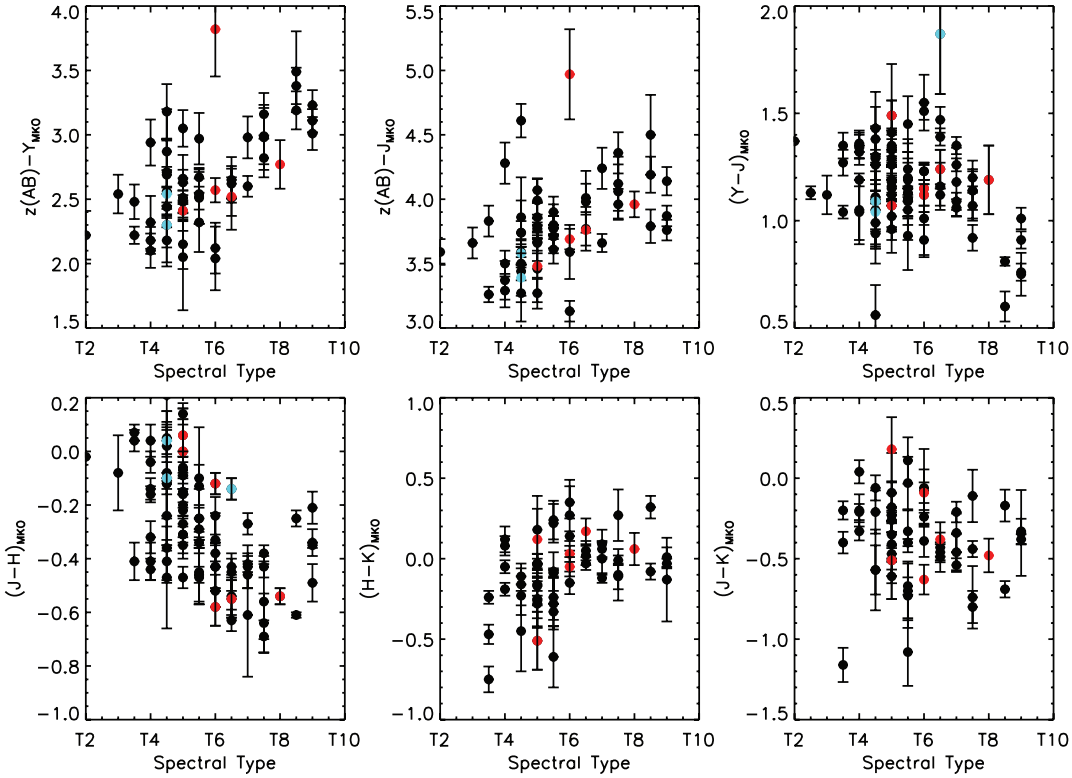

Figure 9. Spectral type versus colour plots for the T dwarfs presented in this paper and all other published T dwarfs from the UKIDSS LAS. T dwarfs classified as peculiar in Section 3 are plotted in the red and blue indicating H_2O-*H*-early and CH_4-*J*-early peculiarities, respectively.

ratio has been modelled through comparison of fields that have been observed in both UKIDSS Deep extragalactic Survey (DXS) and the LAS. This process suggests that at $Y = 20.3$, which corresponds to our $J = 18.8$ limit for T dwarfs with $Y - J = 1.5$, 68 per cent of sources are detected in the LAS. Only 4 per cent of our T dwarfs have $Y - J > 1.5$, and 60 per cent have $Y - J < 1.3$. For this latter group, the DXS–LAS comparison suggests that we are 85 per cent complete at $J = 18.8$. For $J < 18.3$ we can expect to be 97 per cent complete.

To assess if the depth achieved in the DXS overlap fields is typical, and how much scatter there is across LAS DR4, we have also determined the distribution of mean *Y*, *J* and *H* magnitudes for the LAS fields. Approximately 6 per cent of *J*-band fields and 9 per cent of *Y*-band fields have mean magnitudes that are more than 0.3 mag brighter than the mean value for the entire DR4 LAS. Additionally, similar ratios of source counts across the four *YJHK* bands are seen for all fields. We thus conclude that the variation in depth and completeness across the LAS is relatively minor, and that our sample should be complete at the 85 per cent level at its faintest limit.

Our sample has been selected in an identical manner to that of Pinfield et al. (2008), and we follow a similar method for accounting for sources of incompleteness and bias. The selection method is most sensitive to late-T dwarfs, for which $J - H < 0.1$. Through consideration of the SDSS *iz*-selected T dwarfs of Chiu et al. (2006) and Pinfield et al. (2008) demonstrated that we could expect to exclude <10 per cent of ≥T4 dwarfs with this selection. Fig. 9 indicates that this proportion is likely to be much smaller for spectral types ≥T6 (see below). The UKIDSS LAS sample has now grown sufficiently that we are able to select just ≥T6 dwarfs and still have a workable sample size. As such, we now diverge from the treatment of Pinfield et al. (2008) and focus on a sample of ≥T6 dwarfs with $J \leq 18.8$, of which we have identified 25 to date in the LAS.

Since only one ≥T6 dwarf in our sample has $J - H > -0.2$, we proceed on the basis that all such objects have $J - H < 0.1$, and in absence of photometric scatter would be included in our colour selection. However, we have estimated that we could expect one ≥T6 dwarf to be scattered out of our colour selection by photometric measurement errors [2] leading to an estimated sample of 26 ≥ T6 dwarfs.

Since we have obtained spectroscopy for the entire sample that we are considering, we do not need to correct for contaminants that have been scattered into our initial photometric selection, as would be the case for a purely colour-selected sample. However, uncertainties in spectral typing will lead to objects being both scattered out of our sample, and scattered into it. The larger number of detected T5.5 objects compared to T6 objects suggests that with 0.5 subtype uncertainties there should be a small net result of contaminants scattered into our sample. However, we estimate that fewer than one contaminant will be introduced to our sample and we thus neglect this effect from further consideration.

An additional source of incompleteness in our sample arises from the manner in which our selection relies on cross-matching SDSS with UKIDSS. Our selection requires sources to have $z' - J > 3.0$, or to be undetected in SDSS, a status which is established by searching for optical counterparts within 2 arcsec of the UKIDSS sources. The raises the possibility that bona fide candidates which are, in

[2] This was determined by summing probabilities of our *YJH*-selected T dwarfs being scattered beyond the $J - H$ cut-off, based on their 1σ uncertainties in the UKIDSS $J - H$ colours.

reality, non-detections in SDSS will be rejected from our selection if an unrelated optical source is close enough to be misidentified as an optical counterpart. This issue was examined in Pinfield et al. (2008) for the case of UKIDSS–SDSS cross-matching, and a correction of +3 per cent was found to account for this source of incompleteness.

In addition to this effect, the brightest stars effectively mask the sky in both the LAS and SDSS, hiding potential candidates and preventing effective assessment of their optical properties in SDSS. We have estimated that stars with $J < 12.0$ mask a disc on the sky with a typical radius ∼10 arcsec. There are $\sim 10^5$ such stars in UKIDSS LAS DR4, masking less than 1 per cent of the sky from our search method. We thus do not correct for this source of incompleteness.

To allow comparison of our sample to simulations we now remove objects that we know are binary companions to higher mass objects. In our current sample of ≥T6 objects, there is just the T8.5 dwarf Wolf 940B so far identified as a wide companion to a main sequence star. Given that approximately 4 per cent of published T dwarfs are wide companions to higher mass stars (e.g. www.DwarfArchives.org), it is likely that removing this object from our sample is consistent with the required correction.

A further correction is required to account for the inclusion of unresolved binary systems in our magnitude-limited sample, the components of which would fall beyond our $J < 18.8$ cut, were they single objects, but which are included in our magnitude-limited sample because their combined luminosity makes them visible at greater distances. If we define our observed binary fraction as (following Burgasser et al. 2003)

$$\frac{N_{\rm B}}{N_{\rm m}} = \frac{\gamma}{\gamma + 1/{\rm BF} - 1}, \quad (1)$$

where $N_{\rm B}$ and $N_{\rm m}$ are the number of binaries and the total number of sources in our magnitude-limited sample, respectively; BF is the underlying 'true' binary fraction and γ is the fractional increase in volume from which binaries are selected. The fraction of binaries that should be excluded from the sample as they lie beyond the distance suggested by our $J = 18.8$ mag limited is

$$\frac{N_{\rm D}}{N_{\rm B}} = \frac{\gamma - 1}{\gamma}, \quad (2)$$

where $N_{\rm D}$ is the number of binaries that fall within the magnitude limit due to their overluminosity. The fraction of sources that must be excluded from our magnitude-limited sample is thus found as

$$f_{\rm excl} = \frac{N_{\rm B}}{N_{\rm m}} \frac{N_{\rm D}}{N_{\rm B}} = \frac{\gamma - 1}{\gamma + 1/{\rm BF} - 1}. \quad (3)$$

A number of estimates are available for the binary fraction of field and young cluster brown dwarfs (e.g. Burgasser et al. 2003; Pinfield et al. 2003; Maxted & Jeffries 2005; Allen 2007; Lodieu et al. 2007a) ranging from ∼10 to 50 per cent. For our upper limit we take results of the study by Maxted & Jeffries (2005), who used Monte Carlo simulation techniques and the results of published radial velocity surveys to estimate a binary fraction of 32–45 per cent. For our lower limit we use the result of Burgasser et al. (2003), who estimated a binary fraction of 5–24 per cent from high-resolution imaging of field T dwarfs.

Burgasser et al. (2003) derived values for γ based on different assumptions about flux ratio distribution. We will take their values for two extreme cases: that of a flat flux ratio distribution ($\gamma = 1.9$) and the case where all binaries consist of equal flux components ($\gamma = 2\sqrt{2}$). We thus find that we should exclude 3–45 per cent of the sources in our sample to account for the presence of unresolved binarity, resulting in a binary corrected sample of 14–25 ≥T6 dwarfs.

In Pinfield et al. (2008) it was decided that only counting the primary, when most T dwarf binaries appear to be equal-mass binary systems, would incorrectly exclude T dwarf secondaries. The correction that was applied in that case not only excluded binary systems that lay beyond the magnitude limit, but also counted the secondaries of binary systems which lay within the limit. The range of corrections that resulted lie within the range of corrections derived above, so we do not include this consideration in our treatment.

Finally, we apply a correction factor to account for the Malmquist bias. Pinfield et al. (2008) derived a correction by which the sample of T dwarfs was reduced by 12–16 per cent, which results in final estimates of 11–22 (±5) ≥T6 dwarfs with $J < 18.8$ in the 980 deg^2 of DR4 sky.

To allow a convenient comparison with results from 2MASS–SDSS cross-matching (Metchev et al. 2008), the CFBDS (Reylé et al. 2009) and simulations such as those by Burgasser (2004) we now estimate the space density of T6–T9 dwarfs. Table 4 shows the calculated space densities for spectral types between T6 and T9, applying the same corrections to the bins for each subtype as we previously applied to the whole sample. The smaller and larger estimates reflect extremes of the range of possible binary fractions, corrected for Malmquist bias.

Summing the estimates for the T6–T8 range suggests a lower space density limit of $1.3 \pm 0.6 \times 10^{-3}$ pc^{-3}, and an upper limit of $2.5 \pm 1.2 \times 10^{-3}$ pc^{-3}. The uncertainties reflect Poisson noise in the sample, the range of spectral types in each bin and the dispersion of the M_J–spectral type relation of Liu et al. (2006). Our space density

Table 4. Summary of the estimated space densities for our $J < 18.8$ sample of ≥T6 dwarfs. $N_{\rm c}$ refers to corrected numbers based on the sample corrections described in the text, with maximum and minimum values arising from the different possible binary corrections. The values of M_J used to calculate the distance limit and volume probed for each type were calculated using the polynomial relations in M_J versus spectral type derived by Liu et al. (2006), with the exception of the second T9 row, which is calculated assuming the preliminary M_J found for the T9 dwarfs (Smart, private communication). The uncertainties in M_J reflect the rms scatter about the Liu et al. (2006) polynomials and the spectral type uncertainties. The uncertainties in the computed space densities reflect the volume uncertainty that arises from the uncertainty in M_J and Poisson noise in our sample. The minimum and maximum space densities reflect the range encompassed by likely binary fractions (see text).

Type	$T_{\rm eff}$ range (K)	N	$N_{\rm c}$ (min)	$N_{\rm c}$ (max)	M_J (MKO)	Range (pc)	Volume (pc^3)	$\rho_{\rm min}$ ($\times 10^{-3}$ pc^{-3})	$\rho_{\rm max}$ ($\times 10^{-3}$ pc^{-3})
T6–6.5	900–1050	12	5.4 ± 1.6	10.6 ± 3.1	15.05 ± 0.43	56 ± 11	17800 ± 10600	0.30 ± 0.2	0.59 ± 0.39
T7–7.5	800–900	7	3.2 ± 1.2	6.2 ± 2.3	15.64 ± 0.43	43 ± 8	7800 ± 4700	0.40 ± 0.28	0.79 ± 0.55
T8–8.5	650–800	3	1.4 ± 0.8	2.6 ± 1.5	16.52 ± 0.48	29 ± 6	2300 ± 1500	0.58 ± 0.51	1.1 ± 1.0
T9	500–650	3	1.4 ± 0.8	2.6 ± 1.5	17.74 ± 0.53	16 ± 4	400 ± 300	3.1 ± 2.9	6.1 ± 5.7
T9	500–650	3	1.4 ± 0.8	2.6 ± 1.5	17.9 ± 0.50	14 ± 3	300 ± 200	3.9 ± 3.5	7.6 ± 6.9

estimate is lower, but formally consistent with, the value found by Metchev et al. (2008) of $4.7^{+3.1}_{-2.8} \times 10^{-3}$ pc^{-3}.

We provide two estimates for the space density of T9 dwarfs. The first was estimated using a value of $M_J = 17.4$–18.1 (by extending the polynomials of Liu et al. 2006, to later types for the T9–T9.5 range), and so is on the same 'system' as the earlier types. This results in a space density for the T9 dwarfs of 3.1–6.1×10^{-3} pc^{-3}. However, the first parallax measurements for T8+ dwarfs suggest $M_J = 17.6$–18.2 for these objects (Burningham et al. 2009; Smart, private communication). Using these values results in a higher space density of 3.9–7.6×10^{-3} pc^{-3}.

5.2 The simulations

To place constraints on the functional form of the IMF, we now compare our sample to predictions from Monte Carlo simulations of the field brown dwarf population. The simulations we will use are based on those of Deacon & Hambly (2006) and we refer the reader to that work for a detailed description. However, the simulations have been updated in the following ways.

Previous work, such as Burgasser (2004), Deacon & Hambly (2006) and Pinfield et al. (2008) have used the individual object mass function for normalization. While this will produce an accurate representation of the distribution of objects in the stellar luminosity function and the number of objects lying within a survey volume, it does not take into account objects obscured by brighter close binary components and hence will not reflect the potential number of detections from a wide-field search such as this study. We instead use the system mass function normalization 0.0024 pc^{-3} (for objects in the 0.09–0.1 M$_\odot$ range) taken from Deacon, Nelemans & Hambly (2008) which is consistent with the system mass function derived by Chabrier (2005).

Each simulated object was drawn from age and mass probability distributions defined by the various underlying birthrates and mass spectra that were simulated. The mass spectra were of the form

$$\psi(M) \propto M^{-\alpha} \ (\mathrm{pc}^{-3}\,\mathrm{M}_\odot^{-1}). \quad (4)$$

And the expression for the birthrate was of the form

$$b(\tau) \propto \mathrm{e}^{-\beta t}. \quad (5)$$

$T_{\rm eff}$ were determined using the COND evolutionary models of Baraffe et al. (2003). Conversion of these $T_{\rm eff}$ into spectral types however is currently problematic, given the limited number of late-type dwarfs with well-determined parallaxes and good mid-infrared spectral coverage. Furthermore, there is significant scatter in the spectral type-$T_{\rm eff}$ relation for the objects that do have well-determined properties (e.g. Golimowski et al. 2004; Vrba et al. 2004), presumably as a result of the effects of varying composition and surface gravity.

As such, we have used a semi-empirical method for converting the simulated objects' $T_{\rm eff}$ to spectral types. The relevant conversions are given in Table 4, and were determined by reference to Vrba et al. (2004), Golimowski et al. (2004) and more recent studies of T8+ dwarfs by Leggett et al. (2009) and Burningham et al. (2009).

Finally, the simulated population has absolute magnitudes assigned as a function of spectral type using the relations of Liu et al. (2006) for the K band. Colours for each simulated object have been drawn from distribution based on the observed colours of our sample, with an additional scatter of 0.15 mag to account for the fact that the colours of each spectral type do not display a purely Gaussian scatter.

The resulting predictions for the number of ≥T6 dwarfs with $J - H < 0.1$ and $J \leq 18.8$ identified in our search of UKIDSS LAS DR4 for different underlying mass functions and birthrates are given in Table 5. In the relatively near future, the advent of the Wide-field Infrared Survey Explorer (WISE; Wright 2008) and ongoing warm-*Spitzer* programmes will allow comparison of samples such as ours to simulations in a considerably more robust manner. The $H - [4.7]$ colour available from the WISE data set is likely to be as useful a $T_{\rm eff}$ indicator as the $H - [4.5]$ has been (e.g. Warren et al. 2007) in the *Spitzer* era, and these programmes will allow determination of relatively robust $T_{\rm eff}$ for our complete (and future) sample. Thus, the somewhat unsatisfactory conversion of the simulations into spectral type space will no longer be necessary.

It is clear from Table 5 that the number of detected ≥T6 dwarfs is most consistent with a declining mass spectrum (i.e. $\alpha < 0$). This is consistent with the result of Pinfield et al. (2008) which considered an apparently complete sample ≥T4 dwarfs. As mentioned in Section 5.1, our sample may well not be complete for the faintest objects, and a detailed examination of the UKIDSS pipeline, which is beyond the scope of this paper, will be required to assess this issue. However, we would need to only be complete at the ∼30 per cent level to explain our sample size if the underlying mass function were flat or rising. This seems unlikely given that our discussion in Section 5.1 suggests that our sample is likely complete at the ∼85 per cent level. Clearly this result is somewhat dependent on the conversion of our simulations into observational space, and our determination of the form of the IMF will benefit greatly from determination of robust $T_{\rm eff}$ for our entire sample, and the improved absolute magnitude scale for late-T dwarfs that will be obtained from ongoing parallax programmes. At present we have not simulated lognormal forms of the MF, and as such are unable to comment on its likelihood.

Examination of Fig. 10 further supports the conclusion that the negative values of α are to be preferred when only T6–T8 dwarfs are considered. However, the T9 space density appears more consistent with the flat or rising forms for the mass function. It is not

Table 5. Computed numbers of T dwarfs from Monte Carlo simulations of the field population for mass spectra of the form $\psi(M) \propto M^{-\alpha}$ (pc $^{-3}$ M$_\odot^{-1}$); and birthrates of the form $b(\tau) \propto \mathrm{e}^{-\beta t}$.

α	β	N (T6)	N (T7)	N (T8)	N (T9)	N (Tot)
+0.5	0.0	63.3 ± 3.2	26.1 ± 1.6	15.6 ± 1.0	5.8 ± 0.8	111 ± 4
0.0	0.0	36.0 ± 2.0	13.9 ± 1.3	7.7 ± 0.9	2.4 ± 0.4	60 ± 3
−0.5	0.0	22.7 ± 1.4	8.0 ± 0.8	4.0 ± 0.5	1.1 ± 0.3	36 ± 2
−1.0	0.0	15.5 ± 1.5	5.5 ± 0.7	2.4 ± 0.5	0.6 ± 0.2	24 ± 2
−0.5	0.2	24.7 ± 1.8	9.6 ± 1.1	4.9 ± 0.6	1.3 ± 0.4	41 ± 2
−0.5	0.0	22.6 ± 1.8	8.3 ± 0.9	4.1 ± 0.7	1.2 ± 0.3	36 ± 2
−0.5	−0.2	19.7 ± 1.4	6.8 ± 0.8	3.3 ± 0.5	0.9 ± 0.3	31 ± 2
Observed		5.4 – 10.6	3.2 – 6.2	1.4 – 2.6	1.4 – 2.6	11–22

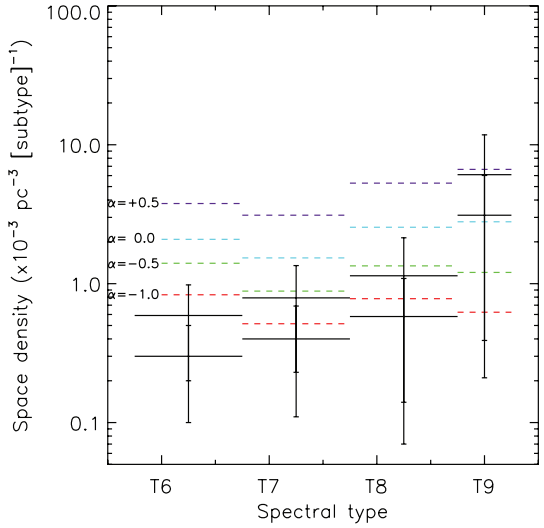

Figure 10. Computed space densities for different spectral types from Monte Carlo simulations of the field population of T dwarfs for a uniform birthrate (i.e. $\beta = 0.0$) and various underlying mass functions that are indicated on the plot. The observed range of space densities is indicated by the solid black lines, with the lower and upper values indicating the range implied by the different likely binary fractions. The T9 space density is that calculated using the relation of Liu et al. (2006) to keep it consistent with the method used to derive observed properties from the simulations. Uncertainties on the maximum and minimum densities are indicated with bars at the mid-point of each spectral type bin, and reflect volume uncertainties and Poisson counting uncertainties.

clear why this is, although the $T_{\rm eff}$ range for T9 dwarfs is even less well determined than for the earlier type objects that we consider, and this may reflect that source of uncertainty. This issue will need to be revisited as the sample grows and properties for these objects become better determined as parallax measurements become available.

Our apparent confirmation of the result of Pinfield et al. (2008), of a declining field mass spectrum in the substellar regime, is in contrast to a number of determinations for the IMF in young clusters and associations, e.g. Upper Sco, 0.3–0.01 $M_\odot$, $\alpha = 0.6 \pm 0.1$ (Lodieu et al. 2007a); Pleiades, 0.48–0.03 $M_\odot$, $\alpha = 0.60 \pm 0.11$ (Moraux et al. 2003); α Per, 0.2–0.04 $M_\odot$, $\alpha = 0.59 \pm 0.05$ (Barrado y Navascués et al. 2002); Blanco 1, 0.6–0.03 $M_\odot$, $\alpha = 0.69 \pm 0.15$ (Moraux et al. 2007) and σ Orionis, 0.5–0.01 $M_\odot$, $\alpha = 0.5 \pm 0.2$ (Lodieu et al. 2009). The reason for this difference in results is not immediately clear, but our result is not unique in this. For example, the result of Metchev et al. (2008) is most consistent with a flat mass spectrum ($\alpha = 0$). It also does not appear to rely solely on our comparison to the simulations based on Deacon & Hambly (2006). Comparison of our computed space densities with the predictions of Burgasser (2004, assuming $T_{\rm eff} = 1050$–650 K for T6–T8 dwarfs) also suggest that our sample size is most consistent with a declining mass spectrum. These results thus suggest that there is a dearth of very cool substellar objects in the local field population compared to what we might expect given the observations of young clusters.

6 SUMMARY

We have reported the discovery of 47 new T dwarfs in the UKIDSS LAS DR4 with spectral types ranging from T0 to T8.5. These bring the total sample of LAS T dwarfs to 80. In assigning spectral types to our objects we have identified eight new spectrally peculiar objects, and divide seven of them into two classes.

H_2O-*H*-early: H_2O-*H* index implies an earlier type than that suggested by the H_2O-*J* index by at least two subtypes.

CH_4-*J*-early: CH_4-*J* index implies an earlier type than that suggested by the H_2O-*J* index by at least two subtypes.

We have ruled out L–T binarity as a sole explanation for both types of peculiarity, and suggest that they may represent hitherto unrecognized tracers of composition and/or gravity. These objects are ideal candidates for further kinematic and mid-infrared studies.

Clear trends in $z'(AB) - J$ and $Y - J$ are apparent for our sample, consistent with weakening absorption in the red pressure broadened wing of the 0.77 μm K I line as temperature decreases through the T sequence.

We have estimated space densities for T6–T9 dwarfs, and by comparing our sample to Monte Carlo simulations have placed weak constraints on the form of the field mass function. Our analysis suggests that negative values of α [where $\psi(M) \propto M^{-\alpha}$ pc^{-3} $M_\odot^{-1}$] are to be preferred. This is at odds with results for young cluster that have generally found $\alpha > 0$. We refrain from making a firm estimate for the value of α in the absence of a more complete examination of the UKIDSS LAS source detection efficiency, and robust $T_{\rm eff}$ estimates for our sample from mid-infrared photometry. However, it seems unlikely that these factors can fully account for our small number of ≥T6 dwarfs, and a declining underlying mass function across the late-T range seems probable.

ACKNOWLEDGMENTS

SKL is supported by the Gemini Observatory, which is operated by AURA, on behalf of the international Gemini partnership of Argentina, Australia, Brazil, Canada, Chile, the United Kingdom and the United States of America. CGT is supported by ARC grant DP0774000. NL acknowledges support from the Ramón y Cajal fellowship number 08-303-01-02. This research has made use of the SIMBAD data base, operated at CDS, Strasbourg, France, and has benefited from the SpeX Prism Spectral Libraries, maintained by Adam Burgasser at http://www.browndwarfs.org/spexprism. Based on observations obtained at the Gemini Observatory, which is operated by the Association of Universities for Research in Astronomy, Inc., under a cooperative agreement with the NSF on behalf of the Gemini partnership: the National Science Foundation (United States), the Science and Technology Facilities Council (United Kingdom), the National Research Council (Canada), CONICYT (Chile), the Australian Research Council (Australia), Ministirio da Ciancia e Tecnologia (Brazil) and Ministerio de Ciencia, Tecnologea e Innovacion Productiva (Argentina). The UKIDSS project is defined in Lawrence et al. (2007). UKIDSS uses the UKIRT WFCAM (Casali et al. 2007) and a photometric system described in Hewett et al. (2006). The pipeline processing and science archive are described in Irwin et al. (2004) and Hambly et al. (2008). This work made use of data obtained on ESO projects 080.C-0090, 081.C-0552 and 082.C-0399, and Gemini projects GN-2007B-Q-26, GN-2008A-Q-15, GN-2008B-Q-2 and GN-2009A-Q-16.

REFERENCES

Allen P. R., 2007, ApJ, 668, 492
Allen P. R., Koerner D. W., Reid I. N., Trilling D. E., 2005, ApJ, 625, 385
Baraffe I., Chabrier G., Barman T. S., Allard F., Hauschildt P. H., 2003, A&A, 402, 701

Barrado y Navascués D., Bouvier J., Stauffer J. R., Lodieu N., McCaughrean M. J., 2002, A&A, 395, 813
Bate M. R., Bonnell I. A., 2005, MNRAS, 356, 1201
Bihain G. et al., 2009, A&A, 506, 1169
Burgasser A. J., 2004, ApJS, 155, 191
Burgasser A. J., Kirkpatrick J. D., Reid I. N., Brown M. E., Miskey C. L., Gizis J. E., 2003, ApJ, 586, 512
Burgasser A. J., McElwain M. W., Kirkpatrick J. D., Cruz K. L., Tinney C. G., Reid I. N., 2004, AJ, 127, 2856
Burgasser A. J., Geballe T. R., Leggett S. K., Kirkpatrick J. D., Golimowski D. A., 2006, ApJ, 637, 1067
Burningham B. et al., 2008, MNRAS, 391, 320
Burningham B. et al. 2009, MNRAS, 395, 1237
Burningham B. et al., 2010, MNRAS, doi:10.1111/j.1365-2966.2010.16411.x
Caballero J. A. et al., 2007, A&A, 470, 903
Casali M. et al., 2007, A&A, 467, 777
Chabrier G., 2002, ApJ, 567, 304
Chabrier G., 2005, in Corbelli E., Palla F., Zinnecker H., eds, Astrophysics and Space Science Library Vol. 327, The Initial Mass Function 50 Years Later, The Initial Mass Function: from Salpeter 1955 to 2005. Springer, Dordrecht, p. 41
Chiu K., Fan X., Leggett S. K., Golimowski D. A., Zheng W., Geballe T. R., Schneider D. P., Brinkmann J., 2006, AJ, 131, 2722
Chiu K. et al., 2008, MNRAS, 385, L53
Dahn C. C. et al., 2002, AJ, 124, 1170
Deacon N. R., Hambly N. C., 2006, MNRAS, 371, 1722
Deacon N. R., Nelemans G., Hambly N. C., 2008, A&A, 486, 283
Delorme P. et al., 2008, A&A, 482, 961
Goldman B., Marsat S., Henning T., Clemens C., Greiner J., 2010, MNRAS, doi:10.1111/j.1365-2966.2010.16524.x
Golimowski D. A. et al., 2004, AJ, 127, 3516
Hambly N. C. et al., 2008, MNRAS, 384, 637
Hewett P. C., Warren S. J., Leggett S. K., Hodgkin S. T., 2006, MNRAS, 367, 454
Hodapp K. W. et al., 2003, PASP, 115, 1388
Irwin M. J. et al., 2004, in Quinn P. J., Bridger A., eds, Proc. SPIE Conf. Ser. Vol. 5493, VISTA Data Flow System: Pipeline Processing for WFCAM and VISTA. SPIE, Bellingham, p. 411
Kendall T. R. et al., T2007, A&A, 466, 1059
Kobayashi N. et al., 2000, in Iye M., Moorwood A. F., eds, Proc. SPIE Vol. 4008, Optical and IR Telescope Instrumentation and Detectors. SPIE, Bellingham, p. 1056
Lawrence A. et al., 2007, MNRAS, 379, 1599
Leggett S. K. et al., 2009, ApJ, 695, 1517
Leggett S. K. et al., 2010, ApJ, 710, 1627
Liu M. C., Leggett S. K., Golimowski D. A., Chiu K., Fan X., Geballe T. R., Schneider D. P., Brinkmann J., 2006, ApJ, 647, 1393
Lodders K., 1999, ApJ, 519, 793
Lodieu N., Hambly N. C., Jameson R. F., 2006, MNRAS, 373, 95
Lodieu N., Dobbie P. D., Deacon N. R., Hodgkin S. T., Hambly N. C., Jameson R. F., 2007a, MNRAS, 374, 372
Lodieu N. et al., 2007b, MNRAS, 379, 1423
Lodieu N., Zapatero Osorio M. R., Rebolo R., Martín E. L., Hambly N. C., 2009, A&A, 505, 1115
Looper D. L., Kirkpatrick J. D., Burgasser A. J., 2007, AJ, 134, 1162
Looper D. L., Gelino C. R., Burgasser A. J., Kirkpatrick J. D., 2008, ApJ, 685, 1183
Lucas P. W., Roche P. F., 2000, MNRAS, 314, 858
Manchado A. et al., 1998, in Fowler A. M., ed., Proc. SPIE Vol. 3354, Infrared Astronomical Instrumentation. SPIE, Bellingham, p. 448
Maxted P. F. L., Jeffries R. D., 2005, MNRAS, 362, L45
Metchev S. A., Kirkpatrick J. D., Berriman G. B., Looper D., 2008, ApJ, 676, 1281
Moraux E., Bouvier J., Stauffer J. R., Cuillandre J., 2003, A&A, 400, 891
Moraux E., Bouvier J., Stauffer J. R., Barrado y Navascués D., Cuillandre J., 2007, A&A, 471, 499
Padoan P., Nordlund Å., 2002, ApJ, 576, 870
Pinfield D. J., Dobbie P. D., Jameson R. F., Steele I. A., Jones H. R. A., Katsiyannis A. C., 2003, MNRAS, 342, 1241
Pinfield D. J. et al., 2008, MNRAS, 390, 304
Reylé C., Delorme P., Delfosse X., Forveille T., Albert L., Willott C., Artigau E., 2009, in Heydari-Malayeri M., Reylé C., Samadi R., eds, SF2A-2009: Proc. Annual Meeting of the French Society of Astronomy and Astrophysics, preprint
Roche P. F. et al., 2003, in Iye M., Moorwood A. F. M., eds, Proc. SPIE Vol. 4841, Instrument Design and Performance for Optical/Infrared Ground-based Telescopes. SPIE, Bellingham, p. 901
Salpeter E. E., 1955, ApJ, 121, 161
Skrutskie M. F. et al., 2006, AJ, 131, 1163
Tinney C. G., Burgasser A. J., Kirkpatrick J. D., 2003, AJ, 126, 975
Vrba F. J. et al., 2004, AJ, 127, 2948
Warren S. J. et al., 2007, MNRAS, 381, 1400
Wright E. L., 2008, in Zinnecker H., Epchtein N., Rauer H. eds, EAS Publ. Ser. Vol. 33, WISE the Wide-field Infrared Survey Explorer. EDP Sciences, p. 57
York D. G. et al., 2000, AJ, 120, 1579
Zapatero Osorio M. R., Béjar V. J. S., Martín E. L., Rebolo R., Barrado y Navascués D., Bailer-Jones C. A. L., Mundt R., 2000, Sci, 290, 103

APPENDIX A: SUMMARY OF FOLLOW-UP OBSERVATIONS

See Tables A1 and A2.

Table A1. Summary of photometric follow-up observations for the T dwarfs presented in this paper.

Object	Filter	Instrument	Date	Total integration (s)	Photometric?	Seeing (arcsec)
ULAS J0150+1359	ESO Z#623	EFOSC2	2008-10-06	1200	n	0.8
	MKO *J*	UFTI	2008-07-04	300	y	0.6
	MKO *H*	UFTI	2008-07-04	900	y	0.6
ULAS J0200+1337	ESO Z#623	EFOSC2	2008-10-07	2400	n	0.9
	MKO *J*	UFTI	2008-07-04	300	y	0.6
	MKO *H*	UFTI	2008-07-04	1800	y	0.6
ULAS J0209+1339	ESO Z#623	EFOSC2	2008-10-07	2400	n	0.9
	MKO *J*	UFTI	2008-07-21	300	y	0.6
	MKO *H*	UFTI	2008-07-21	1800	y	0.6
ULAS J0819+0733	ESO Z#611	EMMI	2007-11-16	1800	y	1
	MKO *Y*	WFCAM	2007-11-17	280	y	0.8
	MKO *J*	WFCAM	2007-11-17	120	y	0.8
	MKO *H*	WFCAM	2007-11-17	1000	y	0.8
	MKO *K*	WFCAM	2007-11-17	1000	y	0.8
ULAS J0840+0759	ESO Z#611	EMMI	2007-11-17	1200	y	1.0
	MKO *J*	WFCAM	2007-11-19	120	y	1.0
	MKO *H*	WFCAM	2007-11-19	1000	y	1.0
ULAS J0842+0936	ESO Z#611	EMMI	2007-11-16	900	y	1.0
	MKO *J*	UFTI	2008-01-13	300	y	0.6
	MKO *H*	UFTI	2008-01-13	1800	y	0.6
	LIRIS K_s	LIRIS	2008-03-16	2200	n	1.0
ULAS J0851+0053	ES0 Z#611	EMMI	2007-11-16	900	y	1.0
	MKO *Y*	WFCAM	2008-01-16	1080	y	0.8
	MKO *J*	WFCAM	2008-01-16	300	y	0.8
	MKO *H*	WFCAM	2008-01-16	1800	y	0.8
	MKO *K*	WFCAM	2008-01-16	1800	y	0.8
ULAS J0853+0006	ESO Z#611	EMMI	2007-11-17	900	y	1.0
	MKO *J*	UFTI	2008-01-22	300	y	0.8
	MKO *H*	UFTI	2008-01-22	1800	y	0.8
	LIRIS K_s	LIRIS	2008-03-16	2400	n	1.0
ULAS J0857+0913	ESO Z#611	EMMI	2007-11-17	900	y	1.0
	LIRIS *J*	LIRIS	2008-03-15	400	n	0.9
	LIRIS *H*	LIRIS	2008-03-15	1200	n	0.9
ULAS J0926+0711	ESO Z#611	EMMI	2008-01-30	900	y	1.0
	MKO *Y*	WFCAM	2008-12-23	540	y	0.6
	MKO *J*	WFCAM	2008-12-23	300	y	0.6
	MKO *H*	WFCAM	2008-12-23	1800	y	0.6
	MKO *K*	WFCAM	2008-12-23	900	y	0.6
ULAS J0926+0835	ESO Z#611	EMMI	2008-01-29	900	y	0.9
	MKO *J*	UFTI	2008-01-17	300	y	0.6
	MKO *H*	UFTI	2008-01-17	1800	y	0.6
	LIRIS K_s	LIRIS	2008-03-16	2400	n	1.0
ULAS J0929+1105	ESO Z#611	EMMI	2008-01-31	1800	y	1.2
	MKO *J*	UFTI	2008-12-24	540	y	0.8
	MKO *H*	UFTI	2007-12-24	3240	y	0.8
ULAS J0943+0858	ESO Z#611	EMMI	2008-01-29	900	y	1.3
	MKO *J*	UFTI	2008-01-08	300	y	1.0
	MKO *H*	UFTI	2008-01-08	1800	y	1.0
ULAS J0943+0942	ESO Z#611	EMMI	2008-01-29	1200	y	1.0
	MKO *J*	WFCAM	2007-11-20	120	y	0.7
	MKO *H*	WFCAM	2007-11-20	1000	y	0.7
ULAS J0945+0755	ESO Z#611	EMMI	2008-01-31	600	y	1.2
	MKO *Y*	WFCAM	2007-12-02	120	y	1.0
	MKO *J*	WFCAM	2007-12-02	120	y	1.0
	MKO *H*	WFCAM	2007-12-02	400	y	1.0
	MKO *K*	WFCAM	2007-12-02	400	y	1.0
ULAS J1012+1021	ESO Z#611	EMMI	2008-01-29	600	y	1.0
	MKO *Y*	WFCAM	2007-12-02	120	y	1.0
	MKO *J*	WFCAM	2007-12-02	120	y	1.0
	MKO *H*	WFCAM	2007-12-02	400	y	1.0
	MKO *K*	WFCAM	2007-12-02	400	y	1.0
ULAS J1034−0015	MKO *J*	UFTI	2009-01-09	300	y	0.8
	MKO *H*	UFTI	2009-01-09	1800	y	0.8

Table A1. *– continued.*

Object	Filter	Instrument	Date	Total integration (s)	Photometric?	Seeing (arcsec)
ULAS J1052+0016	ESO Z#623	EFOSC2	2008-12-24	1800	n	1.0
	MKO *J*	UFTI	2009-01-09	300	y	0.8
	MKO *H*	UFTI	2009-01-09	1800	y	0.8
ULAS J1149−0143	MKO *J*	UFTI	2009-01-07	300	y	0.8
	MKO *H*	UFTI	2009-01-07	1800	y	0.8
ULAS J1153−0147	MKO *Y*	UFTI	2009-01-06	540	y	0.8
	MKO *J*	UFTI	2009-01-06	300	y	0.8
	MKO *H*	UFTI	2009-01-06	1800	y	0.8
	MKO *K*	UFTI	2009-01-06	900	y	0.8
ULAS J1157−0139	MKO *J*	UFTI	2009-01-09	300	y	0.7
	MKO *H*	UFTI	2009-01-09	1800	y	0.7
ULAS J1202+0901	ESO Z#611	EMMI	2008-01-29	600	y	1.0
	MKO *Y*	UFTI	2008-07-15	300	y	0.6
	MKO *J*	UFTI	2008-07-01	300	y	0.7
	MKO *H*	UFTI	2008-07-01	600	y	0.7
	MKO *K*	UFTI	2008-07-15	600	y	0.6
ULAS J1207+1339	MKO *Y*	UFTI	2008-07-15	540	y	0.6
	MKO *J*	UFTI	2008-07-16	300	y	0.6
	MKO *H*	UFTI	2008-07-16	900	y	0.6
	MKO *K*	UFTI	2008-07-15	900	y	0.6
ULAS J1231+0912	ESO Z#623	EFOSC2	2008-05-02	2400	n	1.4
ULAS J1233+1219	ESO Z#611	EMMI	2008-01-30	900	y	0.9
	MKO *Y*	UFTI	2008-07-02	540	y	0.6
	LIRIS *J*	LIRIS	2008-03-15	200	n	0.9
	LIRIS *H*	LIRIS	2008-03-15	600	n	0.9
	MKO *K*	UFTI	2007-07-02	900	y	0.6
ULAS J1239+1025	ESO Z#611	EMMI	2008-01-31	900	y	1.2
	MKO *H*	UFTI	2008-07-17	1800	y	0.5
ULAS J1248+0759	ESO Z#623	EFOSC2	2008-04-30	600	n	1.3
	MKO *Y*	UFTI	2008-07-02	540	y	0.6
	MKO *K*	UFTI	2007-07-02	900	y	0.6
ULAS J1257+1108	ESO Z#623	EFOSC2	2008-04-30	2400	n	1.5
	MKO *J*	UFTI	2008-07-17	300	y	0.5
	MKO *H*	UFTI	2008-07-17	1800	y	0.5
ULAS J1302+1308	ESO Z#623	EFOSC2	2008-06-26	1200	y	2.0
	MKO *Y*	UFTI	2008-07-02	540	y	0.6
	MKO *J*	UFTI	2008-07-01	300	y	0.7
	MKO *H*	UFTI	2008-07-01	900	y	0.7
	MKO *K*	UFTI	2007-07-02	900	y	0.6
ULAS J1319+1209	MKO *Y*	UFTI	2008-06-25	1080	y	1.0
	LIRIS *J*	LIRIS	2008-03-15	400	n	0.9
	LIRIS *H*	LIRIS	2008-03-15	1200	n	0.9
	MKO *K*	UFTI	2008-06-25	1800	y	0.9
ULAS J1320+1029	ESO Z#623	EFOSC2	2008-05-01	600	n	0.9
	MKO *J*	UFTI	2008-07-08	300	y	0.6
ULAS J1326+1200	MKO *Y*	UFTI	2008-07-01	300	y	0.7
	LIRIS *J*	LIRIS	2008-03-16	400	n	0.8
	LIRIS *H*	LIRIS	2008-03-16	1800	n	0.8
	LIRIS K_s	LIRIS	2008-03-16	1800	n	1.0
ULAS J1349+0918	MKO *Y*	UFTI	2008-07-20	2160	y	1.0
	MKO *J*	UFTI	2008-07-19	540	y	0.5
	MKO *H*	UFTI	2008-07-19	3240	y	0.5
	MKO *K*	UFTI	2008-07-20	3240	y	0.9
ULAS J1356+0853	ESO Z#623	EFOSC2	2008-06-26	2700	y	1.5
	MKO *Y*	UFTI	2008-07-06	540	y	0.6
	MKO *J*	UFTI	2008-07-04	300	y	0.6
	MKO *H*	UFTI	2008-07-04	900	y	0.6
	MKO *K*	UFTI	2007-07-06	900	y	0.6
ULAS J1444+1055	MKO *J*	UFTI	2008-07-07	300	y	1.0
	MKO *H*	UFTI	2008-07-07	1800	y	1.0

Table A1. *– continued.*

Object	Filter	Instrument	Date	Total integration (s)	Photometric?	Seeing (arcsec)
ULAS J1445+1257	ESO Z#623	EFOSC2	2008-04-30	3600	n	1.8
	MKO *Y*	UFTI	2008-07-03	1080	y	0.7
	MKO *J*	UFTI	2008-07-04	300	y	0.6
	MKO *H*	UFTI	2008-07-04	1800	y	0.6
	MKO *K*	UFTI	2007-07-03	1800	y	0.7
ULAS J1459+0857	ESO Z#623	EFOSC2	2008-05-01	1200	n	0.9
	MKO *Y*	UFTI	2008-07-05	540	y	0.6
	MKO *J*	UFTI	2008-07-03	300	y	0.7
	MKO *H*	UFTI	2008-07-03	900	y	0.7
	MKO *K*	UFTI	2007-07-05	900	y	0.6
ULAS J1525+0958	MKO *J*	UFTI	2008-07-04	300	y	0.6
	MKO *H*	UFTI	2008-07-04	1800	y	0.6
ULAS J1529+0922	ESO Z#623	EFOSC2	2008-06-26	2400	y	1.3
	MKO *J*	UFTI	2008-07-07	300	y	1.0
	MKO *H*	UFTI	2008-07-07	1800	y	1.0
ULAS J2256+0054	ESO Z#623	EFOSC2	2008-10-07	1200	n	1.7
	LIRIS *J*	LIRIS	2008-09-15	200	y	0.7
	LIRIS *H*	LIRIS	2008-03-16	1200	n	1.0
ULAS J2306+1302	ESO Z#623	EFOSC2	2008-06-26	1200	y	0.8
	MKO *Y*	UFTI	2008-07-03	540	y	0.7
	MKO *J*	UFTI	2008-07-02	300	y	0.6
	MKO *H*	UFTI	2008-07-02	900	y	0.6
	MKO *K*	UFTI	2007-07-03	900	y	0.7
ULAS J2315+1322	ESO Z#623	EFOSC2	2008-10-08	600	n	1.0
	MKO *Y*	UFTI	2008-12-24	540	y	0.8
	LIRIS *J*	LIRIS	2008-09-15	200	y	0.7
	LIRIS *H*	LIRIS	2008-03-16	1800	n	0.8
	MKO *K*	UFTI	2008-12-24	900	y	0.8
ULAS J2318−0013	ESO Z#623	EFOSC2	2008-05-02	2400	y	1.3
	MKO *Y*	WFCAM	2009-07-22	560	y	1.0
	MKO *J*	WFCAM	2009-07-17	200	y	0.8
	MKO *H*	WFCAM	2009-07-17	2000	y	0.8
	MKO *K*	WFCAM	2009-07-22	2000	y	1.0
ULAS J2320+1448	ESO Z#623	EFOSC2	2008-06-26	600	y	0.7
	MKO *Y*	UFTI	2008-07-04	300	y	0.7
	MKO *J*	UFTI	2008-07-02	300	y	0.6
	MKO *H*	UFTI	2008-07-02	600	y	0.6
	MKO *K*	UFTI	2007-07-04	600	y	0.7
ULAS J2321+1354	ESO Z#623	EFOSC2	2008-06-27	1200	y	0.8
	MKO *Y*	UFTI	2008-07-06	300	y	0.6
	MKO *J*	UFTI	2008-07-03	300	y	0.7
	MKO *H*	UFTI	2008-07-03	600	y	0.7
	MKO *K*	UFTI	2007-07-06	600	y	0.6
ULAS J2328+1345	ESO Z#623	EFOSC2	2008-06-27	1800	y	0.8
	MKO *Y*	UFTI	2008-07-08	540	y	0.6
	MKO *J*	UFTI	2008-07-02	300	y	0.6
	MKO *H*	UFTI	2008-07-02	900	y	0.6
	MKO *K*	UFTI	2007-07-08	900	y	0.6
ULAS J2348+0052	ESO Z#623	EFOSC2	2008-12-24	1200	n	1.2
	MKO *Y*	UFTI	2008-07-08	1080	y	0.7
	MKO *J*	UFTI	2008-07-02	300	y	0.6
	MKO *H*	UFTI	2008-07-02	1800	y	0.6
	MKO *K*	UFTI	2007-07-08	1800	y	0.7

Table A2. Summary of spectroscopic follow-up observations for the targets presented in this paper.

Object	Date	Instrument	Grism	Integration time (s)
ULAS J0150+1359	2008-08-22	NIRI	*J*	960
	2009-01-08	IRCS	*HK*	3360
ULAS J0200+1337	2008-08-23	NIRI	*J*	960
ULAS J0209+1339	2008-08-25	NIRI	*J*	960
ULAS J0819+0733	2008-01-22	IRCS	*JH*	2400
ULAS J0840+0759	2008-03-21	NIRI	*J*	1200
ULAS J0842+0936	2008-03-14	NIRI	*J*	960
ULAS J0851+0053	2007-11-27	NIRI	*J*	960
ULAS J0853+0006	2008-01-22	IRCS	*JH*	3600
ULAS J0857+0913	2009-01-08	IRCS	*JH*	3600
	2009-01-08	IRCS	*HK*	3840
ULAS J0926+0711	2009-01-06	NIRI	*J*	960
ULAS J0926+0835	2008-03-21	NIRI	*J*	960
ULAS J0929+1105	2009-03-25	NIRI	*J*	2400
ULAS J0943+0858	2008-01-22	IRCS	*JH*	2400
ULAS J0943+0942	2009-02-26	NIRI	*J*	2400
ULAS J0945+0755	2008-01-22	IRCS	*JH*	1200
ULAS J1012+1021	2008-02-25	NIRI	*J*	1080
ULAS J1034−0015	2009-05-07	IRCS	*JH*	3360
ULAS J1052+0016	2009-01-08	IRCS	*JH*	3600
ULAS J1149−0143	2009-02-23	NIRI	*J*	960
ULAS J1153−0147	2009-02-23	NIRI	*J*	960
ULAS J1157-0139	2009-02-23	NIRI	*J*	960
ULAS J1202+0901	2008-05-25	IRCS	*JH*	2400
ULAS J1207+1339	2008-05-27	IRCS	*JH*	2400
ULAS J1231+0912	2009-05-07	IRCS	*JH*	3360
ULAS J1233+1219	2008-05-07	NIRI	*J*	1440
	2009-12-08	NIRI	*J*	2880
ULAS J1239+1025	2009-07-06	NIRI	*J*	1440
ULAS J1248+0759	2008-05-27	IRCS	*JH*	2400
ULAS J1257+1108	2008-12-05	NIRI	*J*	960
	2009-01-08	IRCS	*HK*	3000
ULAS J1302+1308	2008-05-25	IRCS	*JH*	2400
	2009-02-23	NIRI	*H*	3600
	2009-02-23	NIRI	*K*	3600
ULAS J1319+1209	2008-05-27	IRCS	*JH*	2400
ULAS J1320+1029	2008-05-25	IRCS	*JH*	2400
ULAS J1326+1200	2008-05-27	IRCS	*JH*	2400
ULAS J1349+0918	2008-05-27	IRCS	*JH*	3600
ULAS J1356+0853	2008-05-26	IRCS	*JH*	2400
ULAS J1444+1055	2008-08-11	NIRI	*J*	2400
ULAS J1445+1257	2008-05-26	IRCS	*JH*	3600
ULAS J1459+0857	2008-05-27	IRCS	*JH*	2400
	2008-09-02	NIRI	*H*	2400
	2008-08-29	NIRI	*K*	2250
ULAS J1525+0958	2008-07-05	NIRI	*J*	960
ULAS J1529+0922	2008-08-18	NIRI	*J*	960
ULAS J2256+0054	2008-11-09	IRCS	*JH*	3600
ULAS J2306+1302	2008-07-06	NIRI	*J*	960
ULAS J2315+1322	2008-11-09	IRCS	*JH*	3600
	2008-11-09	IRCS	*HK*	3840
ULAS J2318−0013	2009-12-15	NIRI	*J*	960
ULAS J2320+1448	2008-08-22	NIRI	*J*	960
ULAS J2321+1354	2008-08-23	NIRI	*J*	960
ULAS J2328+1345	2008-08-22	NIRI	*J*	960
ULAS J2348+0052	2008-08-22	NIRI	*J*	960

This paper has been typeset from a TEX/LATEX file prepared by the author.